



# Turbulent momentum and kinetic energy transfer of channel flow over three-dimensional wavy walls

Enwei Zhang <sup>1</sup>, Zhan Wang <sup>1</sup> and Qingquan Liu <sup>2,\*</sup>

<sup>1</sup>*Institute of Mechanics, Chinese Academy of Sciences, Beijing 100190, China*

<sup>2</sup>*School of Aerospace Engineering, Beijing Institute of Technology, Beijing 100081, China*



(Received 1 November 2023; accepted 13 February 2024; published 7 March 2024)

In this paper, we conduct a numerical investigation to analyze the turbulent flow characteristics over three-dimensional wavy walls with varying amplitudes and wavelengths, with a specific focus on the transfer of momentum and kinetic energy. Detailed three-directional momentum statistics are presented to elucidate the influence of shape parameters on flow behavior. The temporal-spatial averaging at relative height is employed to highlight the impact of the wall on mean, time-averaged, and dispersive momentum flux as well as kinetic energy production. Our findings indicate that the current wall amplifies the effects of spanwise momentum flux, which is determined by the transverse flow around the crest. The dispersive shear stress (DSS) demonstrates a notable correlation with vorticity enhancement, while the near-wall vertical momentum flux is jointly governed by the counteraction of Reynolds shear stress and DSS. Through an analysis of kinetic energy conservation, we observe the transfer of kinetic energy among time-averaged, mean, dispersive, and turbulent motions. Overall, kinetic energy is transferred from dispersion to the mean flow and subsequently to turbulence downstream of the crest. On the windward side, both turbulent and dispersive energy are injected into the mean flow, suggesting the possible growth of internal boundary layer. Additionally, the exchange between dispersion and turbulence significantly contributes to turbulent kinetic energy production, particularly in cases with high amplitudes or spanwise wavelengths.

DOI: [10.1103/PhysRevFluids.9.034602](https://doi.org/10.1103/PhysRevFluids.9.034602)

## I. INTRODUCTION

Wall boundaries of various shapes and scales, such as riverbeds in fluvial environments or dunes in landforms, are common in natural settings. The turbulent flow over these three-dimensional (3D) walls exhibits complex and diverse behavior. Understanding the momentum and energy transfer in these complex wall turbulent boundary layers is crucial for comprehending flow patterns and dynamics [1,2].

In fluvial environments, riverbeds display different forms, including ripples [3–6], sand waves, or dunes [7–10], with variations in scale and deformation characteristics. Ripples represent small-scale deformations that act as roughness elements, affecting turbulence close to the wall. On the other hand, large-scale sand waves or dunes have a significant impact on turbulence within the flow depth [11]. Ripples modify the upper turbulent flow by increasing wall resistance, resulting in a downward shift of the velocity profile in the logarithmic region compared with a smooth wall boundary layer. This offset is known as the roughness function [12]. Authors of previous studies

---

\*liuqq@bit.edu.cn

have classified rough walls as transitionally rough or fully rough based on the dimensionless effective roughness height [13]. Parameterization models of the roughness function have been developed through experimental and numerical investigations, establishing relationships between wall shapes, characteristic scales, and effective sand grain roughness height [13–18]. However, the correlation between shape parameters and the roughness function for naturally occurring large-scale sand waves remains a topic requiring further exploration.

Riverbeds can be categorized as two-dimensional (2D) [6,19–22] or 3D [23–28] sand waves based on their morphology. The turbulence over a 2D sand wave is affected by the velocity inflection point resulting from flow separation [29]. The shear layer reconstruction behind the crest exhibits deceleration-acceleration zones, including the deceleration zone from the separation point to the turbulence wake, the acceleration zone associated with the growth of the internal boundary layer, and the outer overlying region far from the wall [30]. This pattern is generally observed in 2D cases, regardless of sand wave morphology or Reynolds number [31]. However, 3D sand waves introduce complexities to momentum transport. Authors of experimental studies have indicated that a 3D riverbed generates higher friction but lower turbulence levels than a 2D case under similar flow conditions [32,33]. Hamed *et al.* [34], through experiments, observed that spanwise heterogeneous walls lead to a sharp reduction in average Reynolds stress due to secondary flows, causing separated fluid to move upward and preventing readherence to the bed surface [11]. These studies have highlighted the distinct impact of 3D walls on turbulence compared with the 2D case. Therefore, understanding the statistical behavior of turbulence over 3D walls is crucial for comprehending the modulation of momentum by these 3D boundaries.

To investigate the effect of wall boundaries on flow over complex terrains, macroscopic turbulence provides insights through temporal-spatial averaging. Spatial averaging decomposes the flow into form-induced quantities, also known as dispersive quantities, which can be used to evaluate flow dispersion mechanisms over complex terrains. Authors of previous studies have utilized the concept of time quadrants to investigate dispersed quadrant events induced by spatial velocity disturbances above rough walls [35,36]. The dispersion mechanism over 2D sand waves exhibits dispersive outward interaction events dominating flow dispersion above the crest, followed by a transition to dispersive sweep events near the separation point. Additionally, dispersive inward interaction and dispersive ejection events control the separation area and windward side, respectively, exhibiting a clockwise transition within one periodic range [35,37,38]. In addition to dispersive velocities, the decomposition separates time-averaged momentum flux or kinetic energy into temporal-spatial averaged and dispersive components, allowing for quantitative estimation through momentum and energy transfer analysis [39–44]. Yuan and Piomelli [43] discovered that the spatial inhomogeneity of Reynolds stresses leads to additional turbulent kinetic energy (TKE) production known as wake (or dispersive turbulent) production. Zampiron *et al.* [45] investigated the partitioning of total kinetic energy through experiments, focusing on small-scale or single-directional roughness such as streamwise ridges. However, further investigation is required to understand flow dispersion and energy transfer mechanisms over 3D large-scale boundaries.

It is worth noting that natural riverbeds can be approximated as 3D wavy walls to some degree, as suggested by Zedler and Street [4] and based on Raudkivi’s [46] summary of fluvial channel geometry. This approximation involves introducing a sinusoidal variation along the spanwise direction of the wavy wall, as shown in Fig. 1. Thus, in this paper, we simplify the riverbeds as large-scale 3D wavy walls with different shape parameters. Large-eddy simulations (LESs) are employed to investigate the turbulence characteristics above these wall boundaries. The subsequent sections of this paper are organized as follows. Section II describes the physical and numerical models. In Secs. III and IV is shown the effect of the shape parameters of the wall on the turbulence field and the macroscopic feature of turbulence through temporal-spatial averaging conduction. The main conclusions are then summarized in Sec. V.

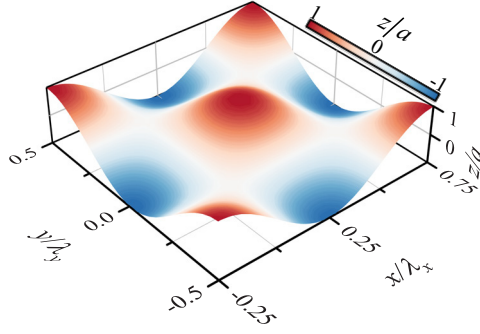


FIG. 1. Elevation of the three-dimensional wavy wall.

## II. PHYSICAL AND NUMERICAL MODELS

### A. Physical model

The present 3D wavy wall is shown in Fig. 1. The elevation of the terrain expresses as

$$\eta = a \sin\left(\frac{2\pi x}{\lambda_x}\right) \cos\left(\frac{2\pi y}{\lambda_y}\right), \quad (1)$$

where  $a$  is amplitude, while  $\lambda_x$  and  $\lambda_y$  represent the streamwise and spanwise wavelengths, respectively.

### B. Numerical model

The LES is used to investigate the present problem. The filtered 3D incompressible Navier-Stokes equations in Cartesian coordinates are

$$\frac{\partial u_i}{\partial x_i} = 0, \quad (2)$$

$$\frac{\partial u_i}{\partial t} + u_j \frac{\partial u_i}{\partial x_j} = -\frac{1}{\rho} \frac{\partial p}{\partial x_i} + \nu \frac{\partial^2 u_i}{\partial x_j \partial x_j} - \frac{\partial \tau_{ij}}{\partial x_j} + \Pi \delta_{li}, \quad (3)$$

where  $i, j = 1, 2, 3$  and repeated indices are implicitly summed over. Here,  $(x_1, x_2, x_3) = (x, y, z)$  respectively denotes the streamwise, spanwise, and vertical coordinates,  $(u_1, u_2, u_3) = (u, v, w)$  denotes filtered velocity components,  $p$  is the filtered pressure,  $\Pi$  is the external force driving the flow,  $\delta_{ij}$  is the Kronecker delta,  $\nu$  is the kinematic viscosity,  $\rho$  is the density, and  $\tau_{ij}$  is the subgrid-scale stress tensor. In this paper, we use a dynamic one-equation to enclose  $\tau_{ij}$  [47]. The transport equation of subgrid-scale kinetic energy can be determined as

$$\frac{\partial k}{\partial t} + u_i \frac{\partial k}{\partial x_i} = -\tau_{ij} \frac{\partial u_i}{\partial x_j} - C_\varepsilon \frac{k^{3/2}}{\Delta} + \frac{\partial}{\partial x_i} \left( \nu_s \frac{\partial k}{\partial x_i} \right), \quad (4)$$

where the subgrid-scale eddy viscosity  $\nu_s = C_k k^{1/2} \Delta$  is determined by the subgrid-scale kinetic energy  $k$ ,  $\Delta = \sqrt[3]{\Delta x \Delta y \Delta z}$  is the filtered grid scale, the subgrid-scale stress is modeled as  $\tau_{ij} = \frac{2}{3} k \delta_{ij} - 2\nu_s S_{ij}$ , with  $S_{ij} = \frac{1}{2} \left( \frac{\partial u_i}{\partial x_j} + \frac{\partial u_j}{\partial x_i} \right)$  being the resolved strain rate tensor, and  $C_k$  and  $C_\varepsilon$  are determined according to the dynamic process proposed by Kim and Menon [47], Ghosal *et al.* [48], and Huang and Li [49]. Therefore, the test filter is used to resolve the kinetic energy, and the similarity assumption is expanded to reduce the complexity of the dynamic process. In this paper, we solve the governing equations in the Cartesian coordinate system. The convection term in the momentum equation is discretized using the second-order upwind difference scheme of the velocity gradient, and the time updating adopts the second-order backward implicit scheme. The PIMPLE

TABLE I. Parameter settings.

Case	$L_x^*$	$L_y^*$	$L_z^*$	$\Delta x^*$	$\Delta y^*$	$\Delta z_{\text{wall}}^*$	$a/\lambda_x$	$a^*$	$\lambda_y/\lambda_x$	$u_\tau \times 10^2$	$\text{Re}_\tau$
G1-1	979	979	550	9.79	9.79	0.49	0.0375	18.36	1	0.5385	275
G1-2	1140	1140	641	11.4	11.4	0.57	0.05	28.57	1	0.6285	321
G1-3	1310	1310	736	13.1	13.1	0.65	0.0625	40.95	1	0.7208	369
G1-4	1500	1500	843	15	15	0.75	0.075	56.35	1	0.8264	423
G1-5	1640	1640	922	16.4	16.4	0.82	0.0875	71.59	1	0.9	460
G1-6	1710	1710	961	17.1	17.1	0.85	0.1	85.28	1	0.9381	480
G2-1	1160	1160	652	11.6	11.6	0.58	0.05	29.10	0.25	0.6403	327
G2-2	1050	1050	590	10.5	10.5	0.52	0.05	26.15	0.5	0.5753	294
G2-3	1140	1140	641	11.4	11.4	0.57	0.05	28.57	1	0.6285	321
G2-4	1060	795	596	10.6	10.6	0.53	0.05	26.50	1.5	0.5831	298
G2-5	1120	1120	630	11.2	11.2	0.56	0.05	28.02	2	0.6164	315
G2-6	1130	1412	635	11.3	11.3	0.56	0.05	28.13	2.5	0.6189	316

algorithm is used for solving the pressure-velocity coupling. It is noted that resolving the smallest turbulent scales is required for direct numerical simulations (DNSs). However, here, we use LESs with a subgrid-scale model to reduce the computation cost. Therefore, to verify the numerical model, in our previous work, we had conducted a numerical simulation of turbulent flow over 2D and 3D wavy walls [50,51]. Through the comparison of mean streamwise velocity and TKE at different streamwise positions with the experimental results by Hamed *et al.* [34], we found the simulation results agree with the experiment, so we believe the present numerical model is reliable.

### C. Simulation configuration

Eleven cases were simulated and divided into two groups (1 and 2), to highlight the impact of wall shape, including amplitude, streamwise wavelength, and spanwise wavelength. Table I provides an overview of these cases. In group 1, denoted as G1-1–G1-6, the streamwise-to-spanwise wavelength ratio was fixed while the amplitude was varied. Conversely, in group 2, referred to as G2-1–G2-6, the ratio of amplitude to streamwise wavelength was fixed while the spanwise wavelength was varied. The Reynolds number is  $\text{Re} = U_0 h / \nu = 4000$ , where  $U_0$  is the bulk velocity and  $h$  is the half height of the channel (noting that the height  $H = 1.125\lambda_x$ ). The corresponding friction Reynolds number  $\text{Re}_\tau = u_\tau h / \nu$  is also shown in Table I, where  $u_\tau$  is the friction velocity determined through the extrapolation of the mean Reynolds shear stress (RSS) from the outer layer. Hamed *et al.* [34] conducted experiments to characterize the flow field at 15 streamwise wavelengths from the inlet, referred to as developed flow conditions. Consequently, we simulated 15 flow periods ( $15\lambda_x/U_0$ ) to develop the turbulence and performed statistical analysis over an additional 50 flow periods. The size of the computational domain is shown in Table I, with  $L_x, L_y, L_z$  denoting the length in streamwise, spanwise, and vertical directions. MacDonald *et al.* [52] investigated the minimal-span channel for rough-wall turbulent flows, which restricted the spanwise channel width to be of the order of a few hundred viscous units. However, in this paper, for group 1, the spanwise length equals  $\sim 1000$ – $1700$  viscous units, as shown in Table I (\* denotes the normalization by viscous unit). For group 2, case G2-4 has  $\sim 800$  viscous units in the spanwise direction, while the rest of the cases have 1100–1400 viscous units in the spanwise direction. Specifically, in our previous work [50], we confirmed that the domain size was sufficiently large to capture the primary flow structure, as demonstrated through the evaluation of the two-point spatial correlation. Periodic boundary conditions were applied in both the streamwise and spanwise directions, while the upper and bottom walls were treated as no-slip boundaries (the upper boundary is a flat wall). In the context of real river flow over wavy dunes, the upper boundary is typically free. Maass and Schumann [53] conducted DNSs of turbulent flow over wavy walls and employed a no-slip wall boundary condition for both the upper and bottom

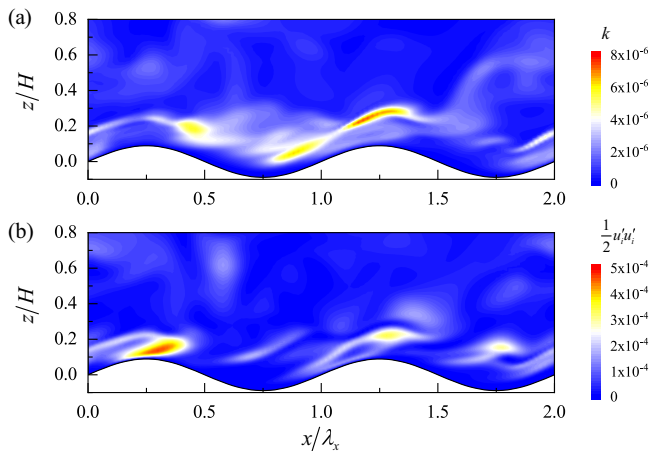


FIG. 2. Comparison of (a) subgrid-scale kinetic energy and (b) resolved turbulent kinetic energy (TKE) of turbulent flow over a three-dimensional wavy wall. The results are shown on the longitudinal section where  $y/\lambda_y = 0$ . The subgrid-scale kinetic energy is approximately two orders of magnitude less than the resolved TKE.

walls. Nakayama and Sakio [54] simulated a similar case but utilized a slip wall boundary condition at the upper wall. Their findings aligned well with the results of Maass and Schumann [53] below the half-height channel region, indicating that the influence of the upper wall on the near-wavy wall region can be disregarded. In this paper, a body-fitted grid was employed, featuring even spacing in the streamwise and spanwise directions while being clustered at the upper and bottom walls using an exponential transformation technique to ensure adequate resolution of the boundary layer. The total number of grid points for most cases is  $N_x \times N_y \times N_z = 101 \times 101 \times 181$ . However, for cases G2-4 and G2-6 in group 2, the grid points are  $N_x \times N_y \times N_z = 101 \times 76 \times 181$  and  $N_x \times N_y \times N_z = 101 \times 126 \times 181$ , respectively. Table 1 presents the grid scale normalized by the viscous length, demonstrating that the grid scale satisfies the requirements for quasi-DNS. In our previous study of turbulent flow over 2D wavy walls [51], we determined that the subgrid-scale quantity could be neglected in comparison with the resolved quantity. Here, we also show the comparison of these two, as shown in Fig. 2. The subgrid-scale kinetic energy is approximately two orders of magnitude less than the resolved TKE. Therefore, the subgrid-scale quantity can be ignored in this paper. This further validates the appropriateness of the chosen grid scales in this paper.

### III. SIMULATION RESULTS

In the subsequent results and discussions, the streamwise wavelength and bulk velocity are used for normalization unless specified. Figures 3(a)–3(c) show the time-averaged velocity on the three-directional sections for case G1-2. The flow behavior behind the crest, induced by the separating flow, leads to a depletion of momentum and consequent alteration of the flow pathway. This modification is observed in the vertical section presented in Fig. 3(a), where the downstream high-velocity streaks exhibit a distinct curved pattern. These curved trajectories highlight the significant role of transverse momentum flux, as evidenced in the transverse section shown in Fig. 3(b). The spanwise velocity within the trough region exhibits a symmetrical structure, influenced by both sides of the crest. This symmetrical flow pattern facilitates the transfer of flow from the spanwise sides of the crest into the trough, thereby amplifying the transverse momentum transfer. Furthermore, Fig. 3(c) illustrates the vertical velocity, clearly indicating the presence of separation and reattachment zones. Specifically, the leeward side exhibits a downward velocity, while the windward side demonstrates an upward velocity.

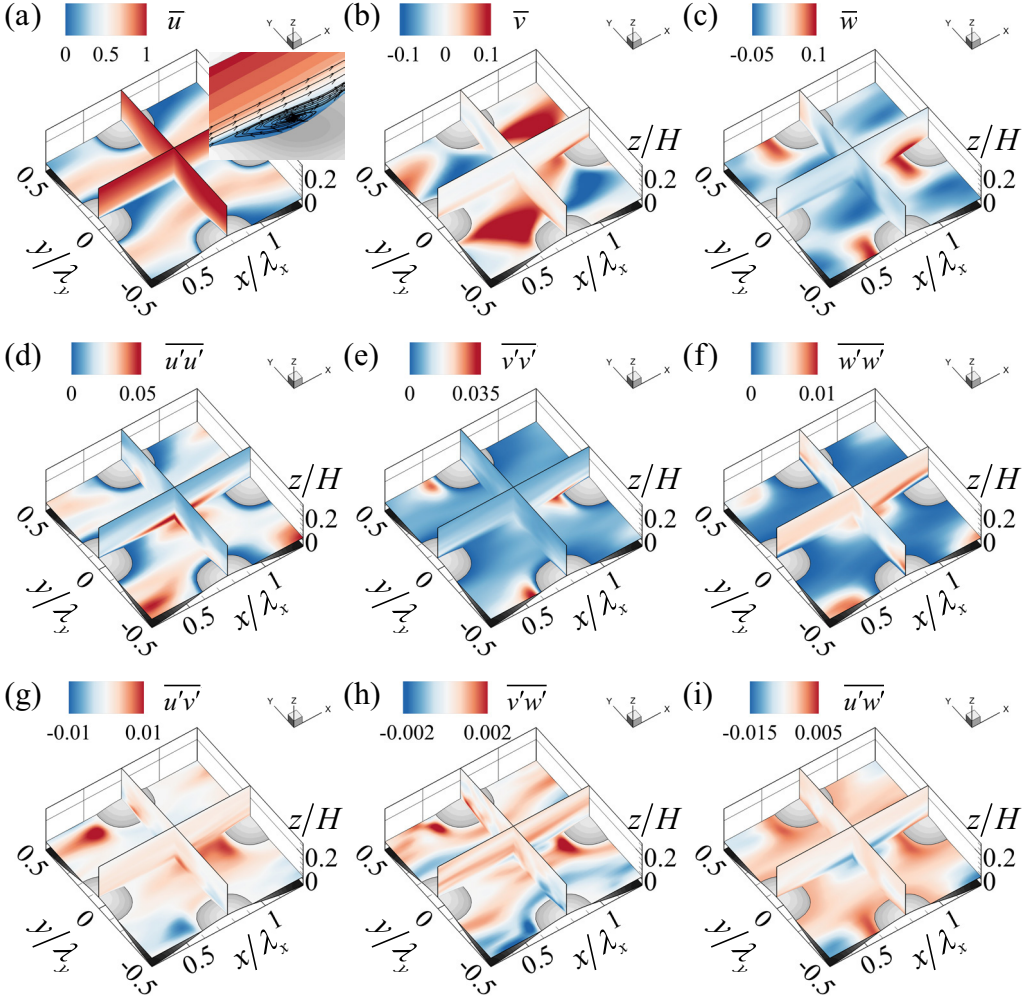


FIG. 3. The turbulence statistics on three-directional sections for G1-2. (a)–(c) Time-averaged velocity, (d)–(f) Reynolds normal stress (RNS), and (g)–(i) Reynolds shear stress (RSS) components.

Figures 3(d)–3(f) show the component of dimensionless Reynolds normal stress (RNS). The longitudinal section in Fig. 3(d) reveals a high streamwise RNS near the crest, which expands downstream, indicating the formation of a turbulent shear layer. In contrast, Fig. 3(e) demonstrates that the spanwise RNS is concentrated in a small region ahead of the crest, highlighting the influence of the terrain on enhancing the spanwise momentum flux. Additionally, Fig. 3(f) suggests that the shear effect plays a crucial role in enhancing the vertical RNS and is closely associated with flow separation. The magnitude of RSS in Figs. 3(g)–3(i) is generally lower than that of the normal stress components. However, certain components verify the significance of the spanwise momentum flux, as illustrated in Figs. 3(g) and 3(h). Here,  $\overline{u'v'}$  and  $\overline{v'w'}$  are both alternated positive-negative patterns, related to the transverse flow around the crest. Furthermore,  $\overline{u'w'}$  features contrarily with streamwise RNS due to the vertical fluctuating velocity. Overall, these momentum statistics are highly dependent on the wall topography, with the spanwise components being significant.

The amplitude parameter significantly influences the magnitude of momentum statistics while leaving their spatial variation unchanged, as illustrated in Fig. 4 for case G1-6. When compared

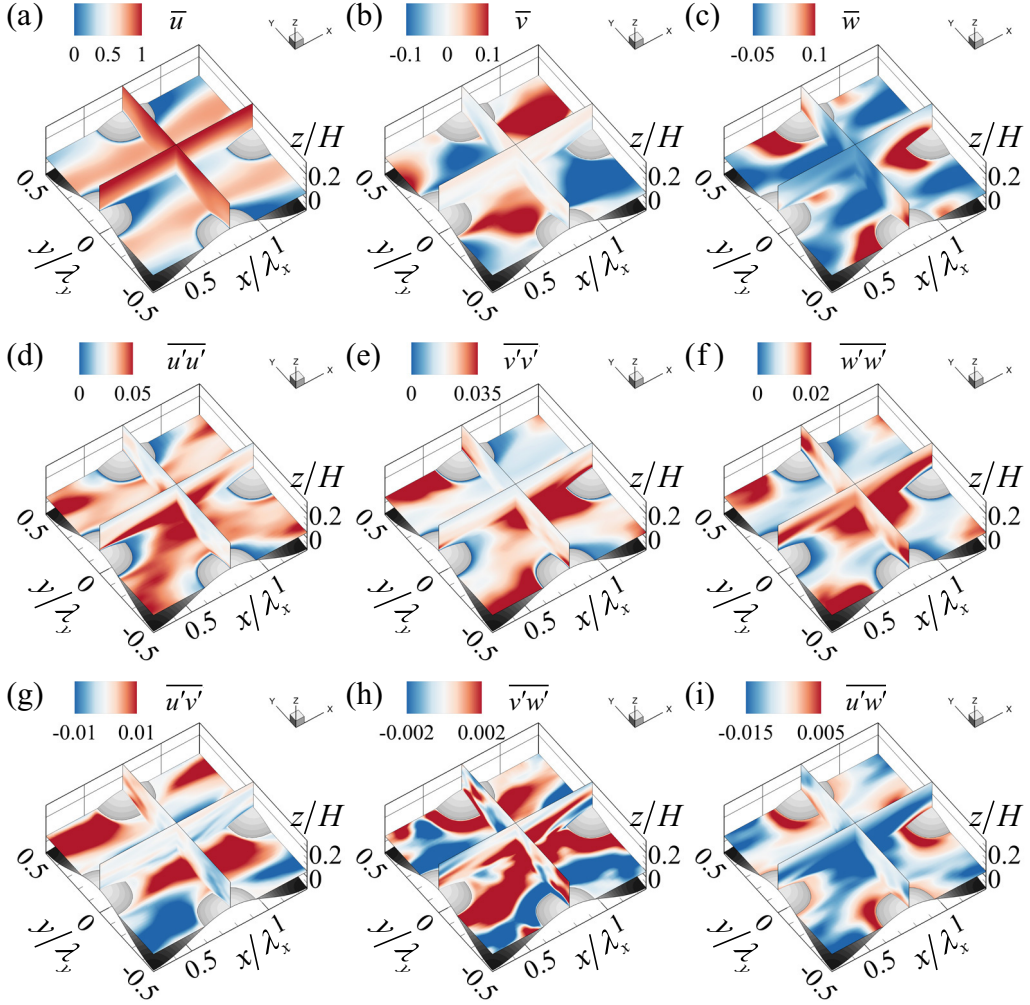


FIG. 4. The turbulence statistics on three-directional sections for G1-6. (a)–(c) Time-averaged velocity, (d)–(f) Reynolds normal stress (RNS), and (g)–(i) Reynolds shear stress (RSS) components.

with case G1-2 in Fig. 3, both the streamwise and spanwise velocities near the wall experience enhancements due to flow separation and transverse flow effects. This intensified flow separation also increases the vertical velocity, as observed in Fig. 4(c). Additionally, the amplitude parameter impacts the magnitude of turbulent stresses. The components of RNS above the trough in Figs. 4(d)–4(f) exhibit a strengthened pattern, indicating that the enhanced turbulent shear layer is generated more readily. In Figs. 4(g)–4(i), the amplitude parameter enhances the magnitude of RSS while maintaining its spatial characteristics unchanged. Consequently, the increase in amplitude amplifies all momentum statistics, attributable to the combined effect of the reinforced turbulent shear layer and transverse momentum transfer.

Figure 5 provides insight into how a case with a high spanwise wavelength (G2-6) influences the turbulence fields. In comparison with case G1-2, the curved streaks observed in G2-6 are interrupted and exhibit a decrease in velocity. Moreover, the enhanced spanwise velocity is predominantly observed on both sides of the crest. Consequently, the region behind the crest shows limited transverse momentum transport. It is important to note that the concentrated area

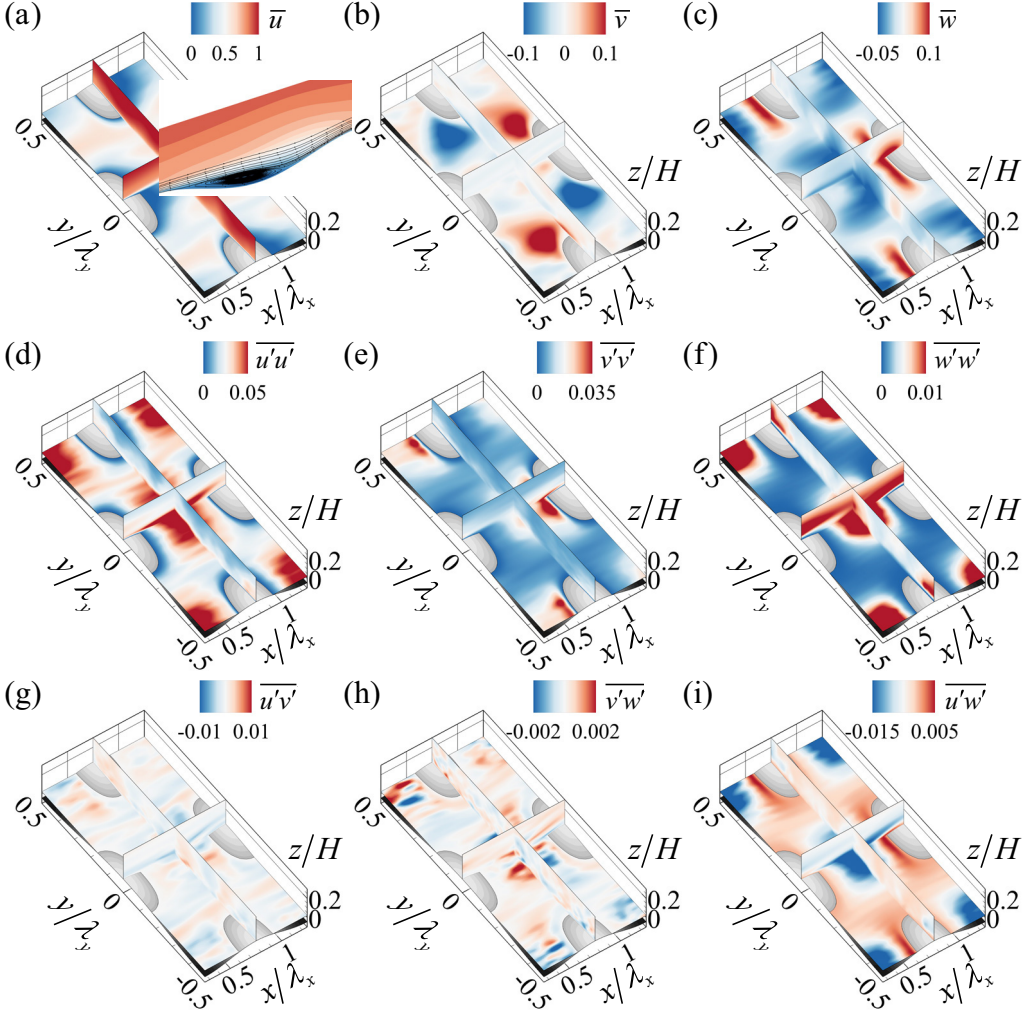


FIG. 5. The turbulence statistics on three-directional sections for G2-6. (a)–(c) Time-averaged velocity, (d)–(f) Reynolds normal stress (RNS), and (g)–(i) Reynolds shear stress (RSS) components.

with a downward (upward) motion in Fig. 5(c) indicates clear flow separation (reattachment), resembling a more 2D scenario. The components of RNS are also affected by this separation, with an increase in streamwise and vertical RNS, while the spanwise RNS weakens. It is also found that  $\overline{u'v'}$  and  $\overline{v'w'}$  distribute dispersedly, while  $\overline{u'w'}$  is significant, akin to a 2D case. Therefore, increased spanwise wavelength limits the spanwise momentum transport and behaves like the 2D situation.

#### IV. ANALYSIS AND DISCUSSION

In rough wall boundary layer flow, the temporal-spatial averaged quantity can better describe the wall effect on the macroscopic turbulent statistics (also known as mean quantity). This approach involves decomposing the instantaneous velocity into

$$u(x, y, z, t) = \bar{u}(x, y, z) + u'(x, y, z, t) = \langle \bar{u}(x, y, z) \rangle + \tilde{u}(x, y, z) + u'(x, y, z, t), \quad (5)$$



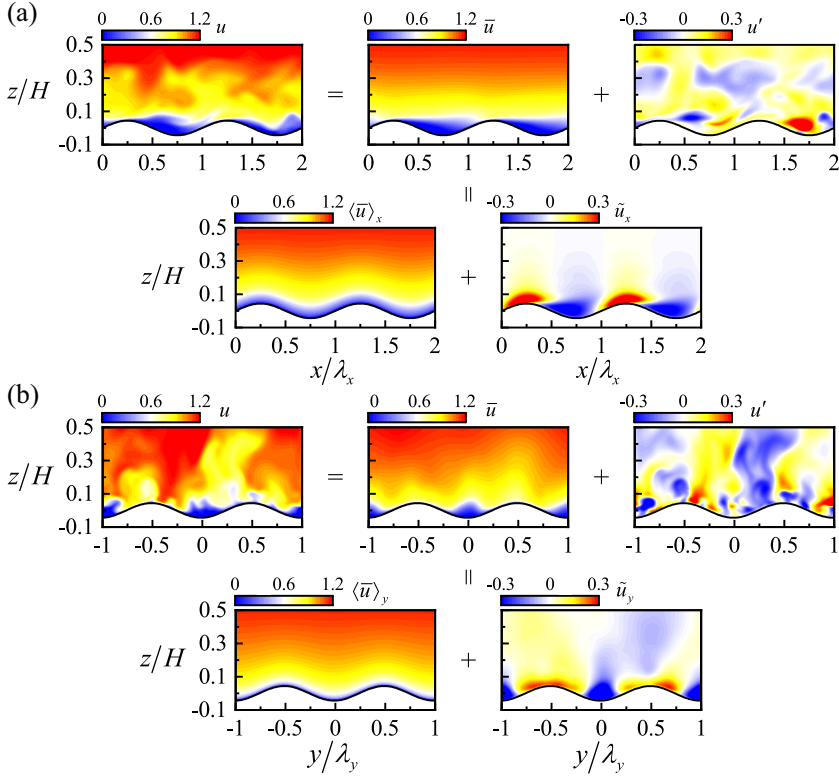


FIG. 6. The schematic of temporal and spatial averaging used in this paper on (a) longitudinal section with  $y/\lambda_y = 0$  and (b) cross-section with  $x/\lambda_x = 0.75$ . (a) The instantaneous streamwise velocity is decomposed into time-averaged and turbulent fluctuating velocities; a spatial averaging along the streamwise direction divides the time-averaged velocity into temporal-spatial averaged velocity and dispersive velocity in the streamwise direction. (b) The decomposition along the spanwise direction. The subscript  $x$  or  $y$  means the spatial averaging along the  $x$  or  $y$  direction.

where  $\bar{u}(x, y, z) = \frac{1}{T} \int_T u(x, y, z, t) dT$  is the time-averaged velocity,  $T$  is the total time for statistical analysis, corresponding to 50 flow periods with  $\sim 12000$  instantaneous snapshots,  $u'(x, y, z, t)$  denotes the temporal fluctuations of velocity, and  $\bar{u}(x, y, z)$  can be further decomposed into temporal-spatial averaged velocity  $\langle \bar{u}(x, y, z) \rangle = \frac{1}{\Omega_i} \int_{\Omega_i} \bar{u}(x, y, z) d\Omega_i$ , which is averaged at the relative height along the spatial domain in both streamwise and spanwise directions and the residual velocity  $\tilde{u}(x, y, z)$  (or the dispersive velocity). Here,  $\Omega_i$  denotes the region of the vertical  $i$ th layer grid along the wavy wall. Notably, the present averaging is conducted at relative height along the streamwise and spanwise directions, which is different from that of Finnigan [55] and Nikora *et al.* [56]. We caution that most previous investigators considered the small roughness and thus carried out double averaging. However, in this paper, we focus on the large-scale topography. This kind of wall boundary leads to typical flow separation, as shown in Fig. 6(a). The streamwise velocity at the trough features a negative value. If we conducted spatial averaging at the absolute height, the temporal and spatial averaging results in negative velocity at the trough while resulting in a positive value at the crest. Therefore, the macrovelocity is difficult to determine. The chosen velocity at the crest ignores the flow separation-induced negative velocity, and the chosen velocity at the trough does not consider the acceleration at the crest. Therefore, we conducted spatial averaging at the relative height to obtain the macrovelocity. This considers both the flow acceleration of the crest and the flow separation of the trough. Figure 6 shows the schematic of temporal-spatial averaging

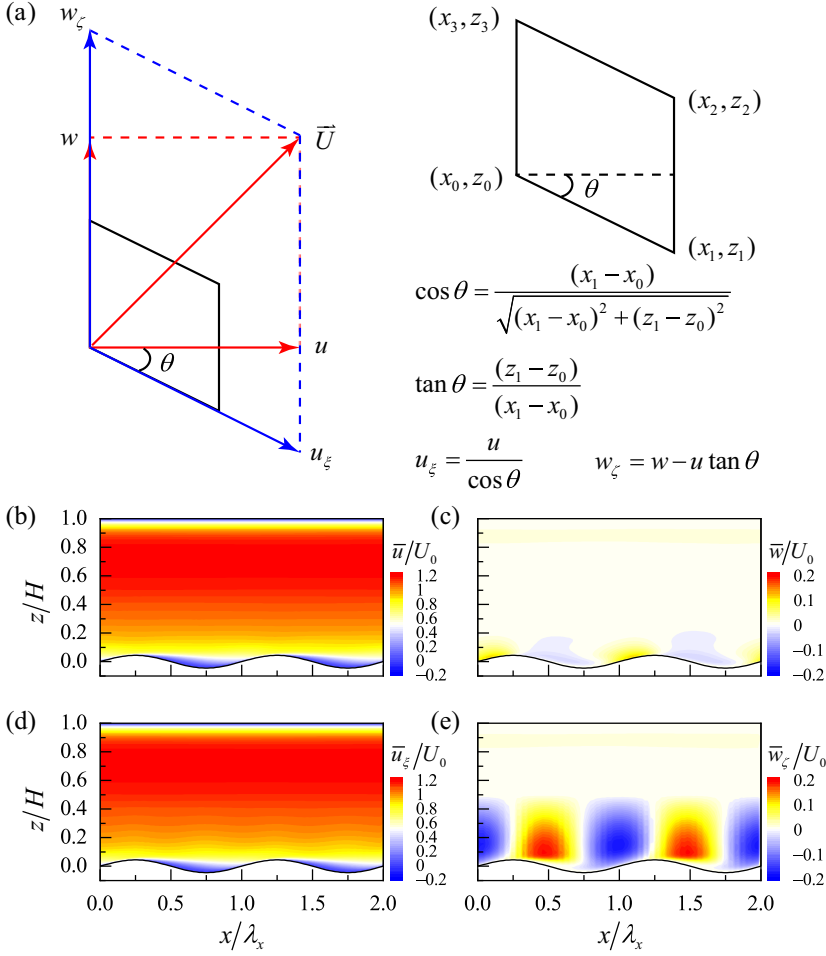


FIG. 7. (a) The transformation from Cartesian to curvilinear coordinate. The time-averaged (b) and (d) streamwise and (c) and (e) vertical velocities shown in (b) and (c) Cartesian and (d) and (e) curvilinear coordinates for case G1-2.

used in this paper. The mean streamwise velocity keeps unvaried at the relative height. Therefore, this quantity can be used to evaluate the macro effect of the wall boundaries.

The present spatial averaging can also be achieved under curvilinear coordinate frame. We further emphasize the difference between these two frames on the longitudinal section ( $y/\lambda_y = 0$ ). First,  $(u, w)$  is defined in the Cartesian coordinates  $(x, z)$ , corresponding to  $(u_\xi, w_\zeta)$  in the curvilinear coordinates  $(\xi, \zeta)$ . Figure 7(a) shows the schematic diagram of the transformation from Cartesian to curvilinear coordinate. The black box shows the spatial grid with four points named  $(x_0, z_0)$ ,  $(x_1, z_1)$ ,  $(x_2, z_2)$ , and  $(x_3, z_3)$ . According to the field decomposition of velocity, there is  $(u_\xi, w_\zeta) = (u/\cos \theta, w - u \tan \theta)$ , where  $\theta$  is the angle between horizontal line and the curvilinear coordinate axis ( $\xi$ ). Figures 7(b)–7(e) show the time-averaged velocities in different frames for case G1-2. The streamwise velocity is basically unvaried in different frames. However, the vertical velocity shows apparent variation, amplified under a curvilinear coordinate frame.

In the subsequent discussion, the vertical momentum flux is emphasized. Therefore, we compare the RSS and dispersive shear stress (DSS) under different frames. According to the relation of

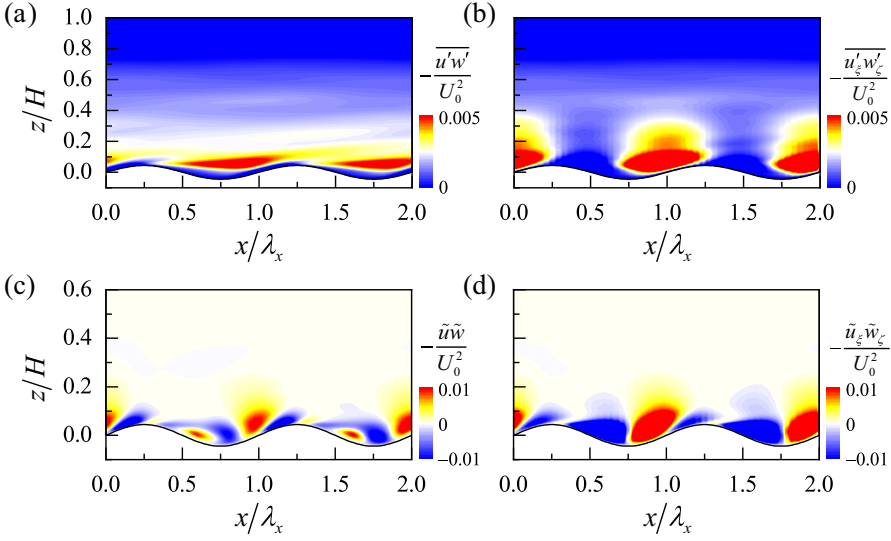


FIG. 8. (a) and (b) Reynolds shear stress and (c) and (d) dispersive shear stress under (a) and (c) Cartesian and (b) and (d) curvilinear coordinates for case G1-2.

$(u_\xi, w_\zeta) = (u/\cos\theta, w - u \tan\theta)$ , the RSS can be transformed into the following formula:

$$\begin{aligned}
 \overline{u'w'} &= \overline{uw} - \overline{u\tilde{w}} = \overline{u_\xi \cos\theta (w_\zeta + u \tan\theta)} - \overline{u_\xi \cos\theta (\tilde{w}_\zeta + \tilde{u} \tan\theta)} \\
 &= \overline{u_\xi w_\zeta} \cos\theta + \overline{u_\xi u} \cos\theta \tan\theta - \overline{u_\xi \tilde{w}_\zeta} \cos\theta - \overline{u_\xi \tilde{u}} \cos\theta \tan\theta \\
 &= (\overline{u_\xi w_\zeta} - \overline{u_\xi \tilde{w}_\zeta}) \cos\theta + (\overline{u_\xi u} - \overline{u_\xi \tilde{u}}) \cos\theta \tan\theta \\
 &= (\overline{u_\xi w_\zeta} - \overline{u_\xi \tilde{w}_\zeta}) \cos\theta + (\overline{uu} - \overline{\tilde{u}\tilde{u}}) \tan\theta \\
 &= \overline{u'_\xi w'_\zeta} \cos\theta + \overline{u'u'} \tan\theta.
 \end{aligned} \tag{6}$$

Therefore, there is  $\overline{u'_\xi w'_\zeta} = \frac{\overline{u'w'}}{\cos\theta} - \overline{u'u'} \frac{\tan\theta}{\cos\theta}$ . Similarly, the DSS in different frames is  $\overline{\tilde{u}_\xi \tilde{w}_\zeta} = \frac{\overline{\tilde{u}\tilde{w}}}{\cos\theta} - \overline{\tilde{u}\tilde{u}} \frac{\tan\theta}{\cos\theta}$ . Figures 8(a) and 8(b) show the comparison of RSS under different coordinate frames. The RSS under the Cartesian coordinate is more apparent, with enhancement above the trough due to the strong shear layer. Under curvilinear coordinates, however, RSS highly varies, with enhanced positive value on the windward side.

Figures 8(c) and 8(d) show the DSS in different frames. The pattern of DSS along the wall is basically insensitive to the frames. However, there is a minor difference behind the crest. The slightly positive DSS under the Cartesian coordinate changes into a negative value in a curvilinear frame. This arises due to the variation of dispersive vertical velocity (not shown here). According to the results in Figs. 8(c) and 8(d), we infer that the curvilinear coordinate might change the variation of high-order statistics. In fact, authors of previous studies have widely found that it is common that the RSS has a negative value on the windward side for 2D wavy wall turbulence. Hudson *et al.* [57] and Cherukat *et al.* [58] pointed out that the negative value of RSS is an artifact of using the Cartesian coordinate system and would be positive under a curvilinear coordinate system. However, Yang and Shen [59] attributed the negative value to vertically bent quasistreamwise vortices on the windward side. In our previous work, we also verified the quasistreamwise vortex pair shown in the Cartesian coordinate frame contributes to the negative RSS on the windward side [51]. Therefore, the Cartesian coordinate shows the results more intuitively. The subsequent results and discussions are based on this frame.

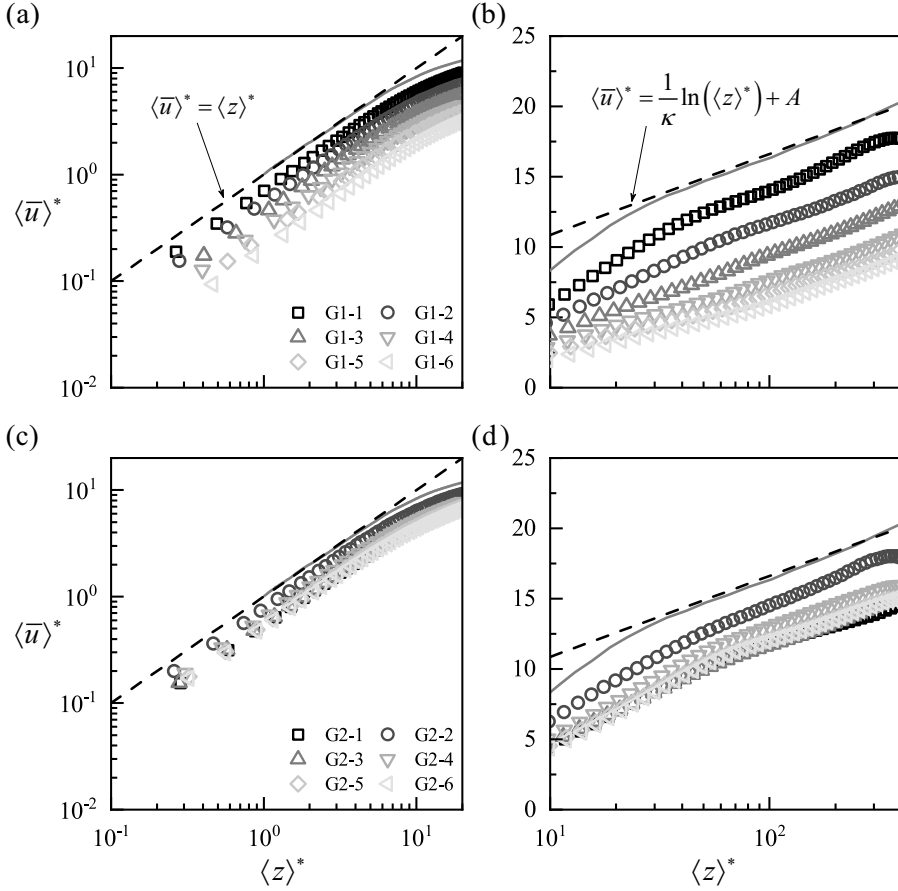


FIG. 9. The profiles of mean streamwise velocity at the (a) and (c) logarithmic and (b) and (d) semilogarithmic plots. (a) and (b) Group 1; (c) and (d) group 2.

### A. Profiles of the mean streamwise velocity

Figure 9 shows the mean streamwise velocity profiles; the asterisk denotes the normalization by friction velocity, where  $\langle \bar{u} \rangle^* = \langle \bar{u} \rangle / u_\tau$  and  $\langle z \rangle^* = \langle z \rangle u_\tau / \nu$ . Figures 9(a) and 9(c) demonstrate that the velocity profiles conform to a linear law within the viscous sublayer  $\langle z \rangle^* < 5$ . However, these profiles exhibit lower values than a flat-wall boundary layer (indicated by the gray dashed line). Increasing the amplitude of the wall shape leads to a downward shift in the velocity profile. On the other hand, raising the spanwise wavelength initially results in an upward shift of the profile, followed by a subsequent downward shift.

In the region  $\langle z \rangle^* > 50$ , as shown in Figs. 9(b) and 9(d), a typically logarithmic law can be observed. The logarithmic law of the mean velocity with the distance from the wall is expressed as

$$\langle \bar{u} \rangle^* = \frac{1}{\kappa} \ln(\langle z \rangle^*) + A, \quad (7)$$

where  $A$  is a parameter that depends on the roughness of the surface, with  $A = 5.1$  chosen for a flat-wall boundary layer flow, and  $\kappa \approx 0.4$  is the von Karman constant. The increase in amplitude shifts the profile downward, while the increase in spanwise wavelength for current cases shifts the profile upward and then downward.

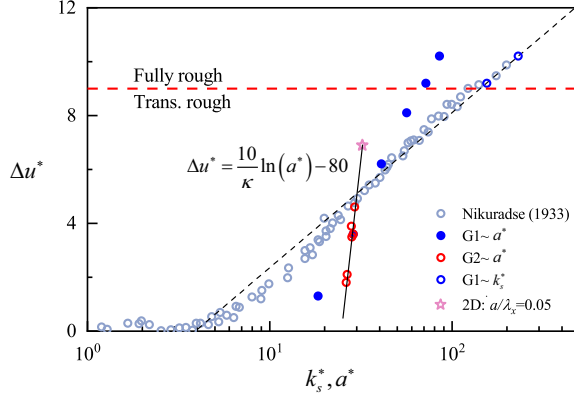


FIG. 10. Roughness function.

We construct the relation between the wall shape and roughness to emphasize the wall effect on macroscopic flow. For turbulent flow over a rough wall, the logarithmic law is written as

$$\langle \bar{u} \rangle^* = \frac{1}{\kappa} \ln(\langle z \rangle^*) + A - \Delta u^*. \quad (8)$$

For a fully rough regime, Eq. (8) should meet the requirement [60]:

$$A - \Delta u^* + \frac{1}{\kappa} \ln(a^*) = B, \quad (9)$$

where  $B$  is the intercept constant determined by the specific roughness form and  $\Delta u^*$  is the roughness function. For this paper,  $a^*$  is the dimensionless amplitude.

Figure 10 shows the roughness function varied with dimensionless amplitude. The effective sand grain height  $k_s^*$  is also shown. The intercept constant  $B = 8.5$  was determined by Flack and Schultz [61], also known as the Nikuradse constant [62]. For a fully rough regime, the roughness function is

$$\Delta u^* = \frac{1}{\kappa} \ln(k_s^*) - 3.4. \quad (10)$$

A red dashed line at  $\Delta u^* = 9$  marks the approximate start of the fully rough regime [12]. It is seen that cases G1-5 and G1-6 belong to the fully rough regime, while cases G1-1–G1-4 belong to the transitionally rough regime. The relations between the effective sand grain height and amplitude for G1-5 and G1-6 are  $k_s^* = 2.16a^*$  and  $2.7a^*$ . However, it should be noted that all cases in group 2 fall within the transitional rough regime. Additionally, we include a plot of the limiting spanwise-wavelength case (or the 2D wavy wall case) using data from our previous work [38]. Our analysis reveals that the current roughness function does not exceed that of the 2D wavy wall case. Furthermore, the roughness function aligns well with the universal logarithmic law.

### B. The vertical momentum flux (shear stress)

The shear stress can also be divided into Reynolds and dispersive stresses via temporal-spatial averaging. Here, we consider the streamwise momentum conservation equation in 2D:

$$\begin{aligned} \frac{\partial \langle \bar{u} \rangle}{\partial t} + \frac{\partial}{\partial x} \left( \langle \bar{u} \rangle \langle \bar{u} \rangle + \langle \overline{u'u'} \rangle + \langle \tilde{u}\tilde{u} \rangle - \nu \frac{\partial \langle \bar{u} \rangle}{\partial x} \right) \\ + \frac{\partial}{\partial z} \left( \langle \bar{u} \rangle \langle \bar{w} \rangle + \langle \overline{u'w'} \rangle + \langle \tilde{u}\tilde{w} \rangle - \nu \frac{\partial \langle \bar{u} \rangle}{\partial z} \right) = -\frac{1}{\rho} \frac{\partial \langle \bar{p} \rangle}{\partial x}. \end{aligned} \quad (11)$$

The first term on the left side of Eq. (11) can be ignored due to the statistically steady flow. Equation (11) can be rewritten as

$$\begin{aligned} & \frac{\partial}{\partial x} \left( -\langle \bar{u} \rangle \langle \bar{u} \rangle - \langle \overline{u'u'} \rangle - \langle \tilde{u}\tilde{u} \rangle + \nu \frac{\partial \langle \bar{u} \rangle}{\partial x} \right) \\ & + \frac{\partial}{\partial z} \left( -\langle \bar{u} \rangle \langle \bar{w} \rangle - \langle \overline{u'w'} \rangle - \langle \tilde{u}\tilde{w} \rangle + \nu \frac{\partial \langle \bar{u} \rangle}{\partial z} \right) = \frac{1}{\rho} \frac{\partial \langle \bar{p} \rangle}{\partial x}. \end{aligned} \quad (12)$$

Equation (12) suggests that the vertical momentum flux is balanced not only by its components including spatial-averaged RSS, DSS, and viscous shear stress (VSS), but streamwise momentum flux also contributes to the momentum conservation. This arises due to the present method of temporal and spatial averaging. The present averaging can also be achieved in the curvilinear coordinate, and thus, we can ignore the first term of Eq. (12). However, this leads to additional terms. Since the Cartesian coordinate shows the results more directly, we utilize this framework to emphasize the momentum transfers. Here, the vertical momentum flux is highlighted, the total vertical momentum flux (or stress) consists of spatial-averaged RSS, DSS, and VSS:

$$\langle \bar{\tau}_t \rangle = -\langle \overline{u'w'} \rangle - \langle \tilde{u}\tilde{w} \rangle + \nu \frac{\partial \langle \bar{u} \rangle}{\partial z}, \quad (13)$$

where  $\langle \bar{\tau}_t \rangle$  is the total shear stress (TSS).

Figure 11 shows the dimensionless RSS  $-\overline{u'w'}$ , DSS  $-\tilde{u}\tilde{w}$ , VSS  $\bar{\tau}_v = \nu \partial \bar{u} / \partial z$ , and TSS  $\bar{\tau}_t$  on characterized cross-section. For cases with higher amplitudes,  $-\overline{u'w'}$  exhibits an increase in magnitude and extent within the trough region, as depicted in Figs. 11(a1) and 11(b1). A slight negative  $-\overline{u'w'}$  near the crest in Fig. 11(b1) can be attributed to the presence of a counterrotating vortex pair, as discussed by Zhang *et al.* [38]. The reduction in turbulence intensity is responsible for the acceleration of the flow along the curved streaks, as observed in Fig. 3, leading to weakened  $-\overline{u'w'}$  in areas where the boundary exhibits zero-streamwise curvature. Figures 11(a1) and 11(c1) indicate that an increased spanwise wavelength enhances the magnitude of  $-\overline{u'w'}$  due to the presence of pronounced separated shear.

The magnitude of  $-\tilde{u}\tilde{w}$  is comparable with that of  $-\overline{u'w'}$ . Notably, there is a conspicuous increase in negative  $-\tilde{u}\tilde{w}$  magnitude within the trough region as the amplitude increases, as depicted in Figs. 11(a2) and 11(b2). This region corresponds to areas where the flow exhibits higher vertical velocity and lower spanwise velocity, as observed in Fig. 3. Conversely, positive  $-\tilde{u}\tilde{w}$  is present in regions where the flow displays higher spanwise velocity and lower vertical velocity in Fig. 3. These observations suggest a correlation between  $-\tilde{u}\tilde{w}$  and spanwise/vertical motions. The  $\bar{\tau}_v$  in Figs. 11(a3)–11(c3) demonstrates its predominant contribution within the near-wall region. The  $\bar{\tau}_t$  in Figs. 11(a4)–11(c4), encompassing  $-\overline{u'w'}$ ,  $-\tilde{u}\tilde{w}$ , and  $\bar{\tau}_v$ , is primarily generated through the interaction between  $-\overline{u'w'}$  and  $-\tilde{u}\tilde{w}$ .

Figure 12 presents the vertical profiles of the shear stress components, which are dimensionless by the friction velocity. The interplay between  $-\langle \overline{u'w'} \rangle^*$  and  $-\langle \tilde{u}\tilde{w} \rangle^*$  aligns with the observations by Zampiron *et al.* [45]. The increase in  $-\langle \overline{u'w'} \rangle^*$  is counterbalanced by a decrease in  $-\langle \tilde{u}\tilde{w} \rangle^*$ , as depicted in Figs. 12(a), 12(b), 12(d), and 12(e). Furthermore, the current bulk Reynolds number dominates the viscosity near the wall, thereby influencing the impact of the  $\langle \bar{\tau}_v \rangle^*$  within the sublayer. In Fig. 12(a), the increase in amplitude raises the peak position of  $-\langle \overline{u'w'} \rangle^*$  while maintaining its magnitude. Conversely, the increase in spanwise wavelength in Figs. 12(d) and 12(e) amplifies the peak value of  $-\langle \overline{u'w'} \rangle^*$  without affecting its peak position, indicating the strengthening of the shear layer in a 2D scenario (where a larger spanwise wavelength indicates the wall being closer to a 2D state). Likewise, a similar trend can be observed for  $-\langle \tilde{u}\tilde{w} \rangle^*$  in Figs. 12(d) and 12(e). The presence of the wall boundary generally affects the macroscopic vertical momentum flux through the induced turbulent shear layer. The higher RSS (DSS) is primarily attributed to the occurrence of shear in this context.

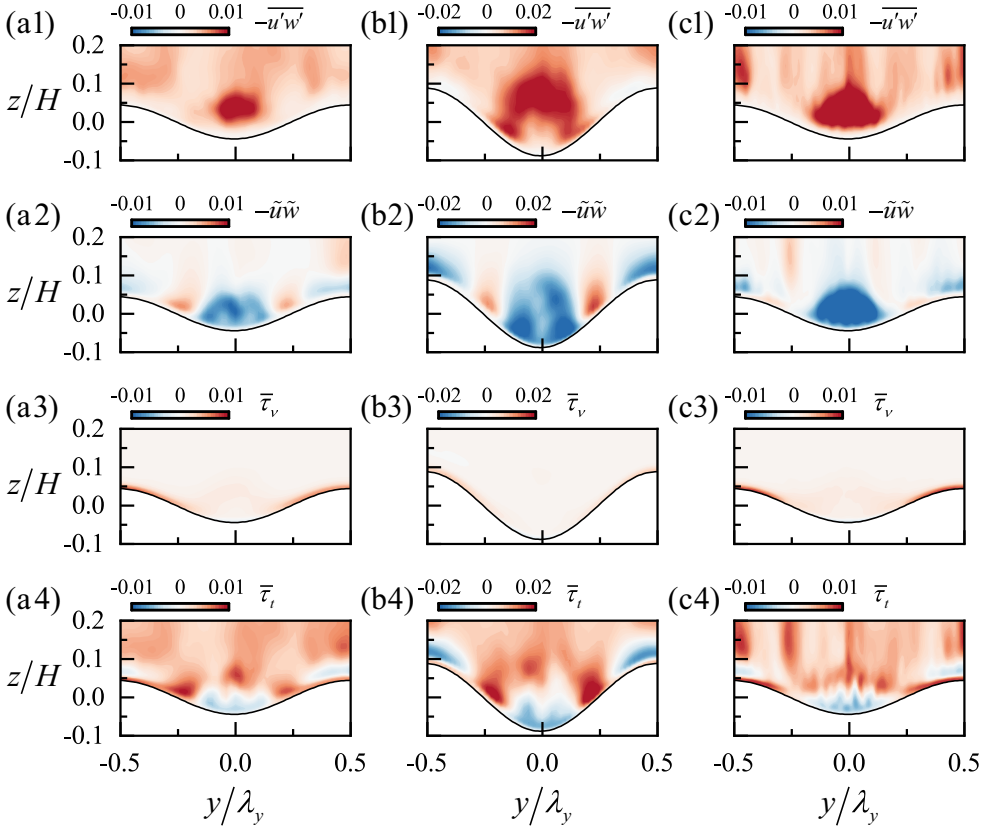


FIG. 11. The Reynolds shear stress (RSS), dispersive shear stress (DSS), viscous shear stress (VSS), and total shear stress (TSS) on the cross-section for cases (a) G1-2, (b) G1-6, and (c) G2-6.

### C. Spatial quadrant of DSS and its activation mechanism

We next emphasize the DSS composition based on the quadrant distribution. The DSS can be divided into  $Q_{d1}(\tilde{u} > 0, \tilde{w} > 0)$ ,  $Q_{d2}(\tilde{u} < 0, \tilde{w} > 0)$ ,  $Q_{d3}(\tilde{u} < 0, \tilde{w} < 0)$ , and  $Q_{d4}(\tilde{u} > 0, \tilde{w} < 0)$ , corresponding to dispersive outward interaction, ejection, inward interaction, and sweep events, respectively.

Figure 13 shows the DSS on three-directional sections (XS1, YS1, and ZS1 denote the section at  $x/\lambda_x = 0.75$ ,  $y/\lambda_y = 0$ , and  $z/a = 0.5$ ) for G1-3, and the dispersive velocity is identified by the isolines to show the spatial quadrant. On the YS1 section, as shown in Fig. 13(a), the DSS exhibits alternating positive and negative values along the streamwise direction. In the R1 region, the DSS is predominantly influenced by  $Q_{d3}$ . This characteristic continues downstream into the R3 region. On the other hand, in the R2 and R4 regions,  $Q_{d2}$  governs the behavior of the DSS, which could be attributed to the formation of vortices. Furthermore, the presence of R5, characterized by  $Q_{d1}$ , aligns with the findings of Dey *et al.* [37]. Along the spanwise direction, the alternation of positive and negative DSS can also be observed, as shown in Fig. 13(c). In R3,  $Q_{d3}$  occupies a significant portion of the trough region, forming a closed annular area around R2. Additionally,  $Q_{d1}$  in R5 expands transversely. These characteristics are consistently observed across variations in amplitude.

Figure 14 shows the DSS for G2-6. Like Fig. 13, the spatial pattern of DSS remains unchanged. A higher spanwise wavelength leads to a weakening and narrowing of the dispersive ejection in R2 and

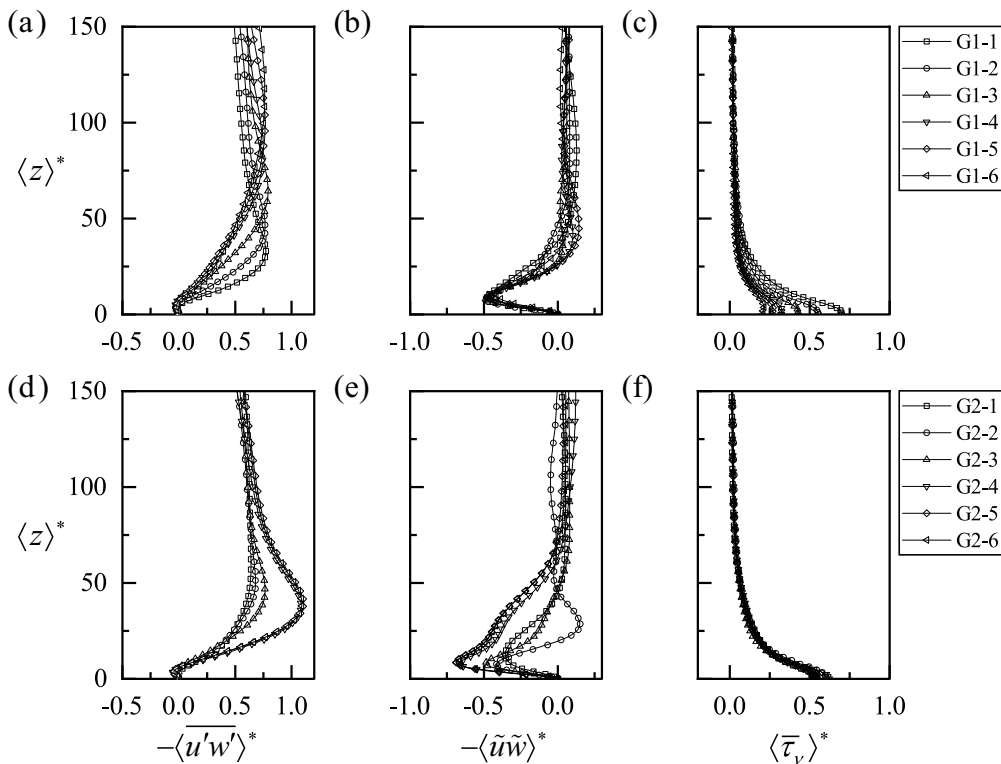


FIG. 12. The dimensionless spatial-averaged Reynolds shear stress (RSS), dispersive shear stress (DSS), and viscous shear stress (VSS) profiles.

R4. However, in R3, the dispersive inward interaction intensifies due to apparent flow separation. (It is important to note that the parameters for G1-3 and G2-6 differ in both amplitude and spanwise wavelength, so a strict comparison is not established. We also obtained results for G1-2, which are qualitatively like those of G1-3.) The enhanced dispersive inward interaction is evident in the cross-section depicted in Fig. 14(b). In curved streaks characterized by high streamwise velocity, such as R6, the DSS is relatively weak due to the limitations imposed by the transverse flow around the crest.

The significance of the DSS contribution in the near-wall region is notable. As one moves vertically away from the wall, the phase modulation between streamwise and vertical velocities leads to a weaker DSS until its effect diminishes completely. In Fig. 13(a), on the windward side, the phase difference between streamwise and vertical velocities is  $\sim 0.25\lambda_x$ . This phase difference along the spanwise direction is also evident, as shown in the cross-section. Conversely, for G2-6 in Fig. 14, there is no apparent phase difference, resulting in a weaker DSS in R6. Consequently, the presence of the wall in this paper influences the dispersion of flow by modulating the phase difference between streamwise and vertical dispersive velocities, thereby activating the region associated with DSS.

In the case of a limiting spanwise wavelength or a 2D wavy wall scenario, the DSS exhibits a quadrant conversion of  $Q_{d4} - Q_{d3} - Q_{d2} - Q_{d1}$  along one wavelength, as reported by Zhang *et al.* [38]. Figure 15 provides a comparison of the DSS between the current case, G1-2, and a 2D wavy wall scenario under the same amplitude conditions. The results for the 2D wavy wall case are derived from our previous work [38]. The spanwise heterogeneity weakens the occurrences of  $Q_{d3}$  and  $Q_{d1}$  events in R3 and R5. In R1, the presence of a 2D wavy wall induces  $Q_{d4}$ , contrasting with



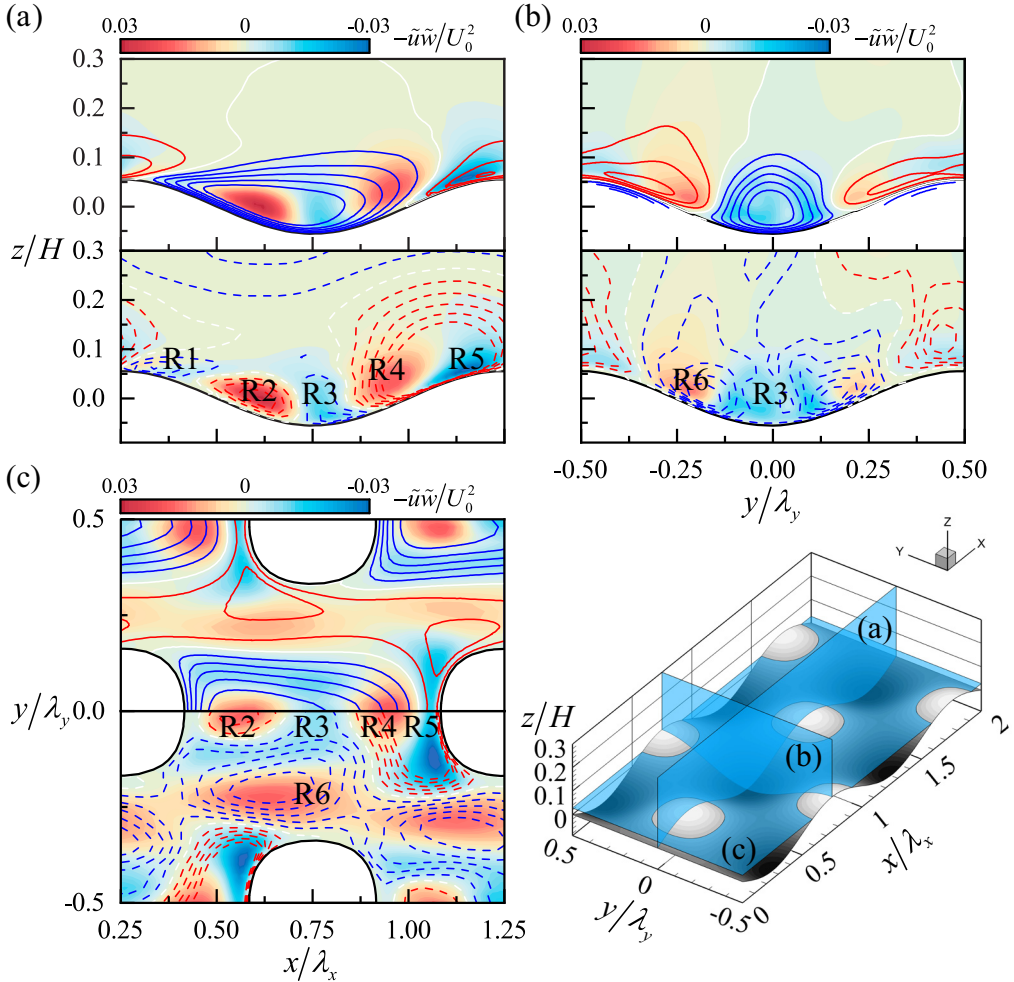


FIG. 13. The contours of dispersive shear stress (DSS) and isolines of dispersive velocity components for G1-3 on (a) YS1, (b) XS1, and (c) ZS1 sections. The solid and dashed lines are the dispersive streamwise and vertical velocities, with blue (red) denoting less (larger) than zero.

$Q_{d3}$  observed in 3D wavy wall turbulence. This suggests that the spanwise heterogeneity fails to trigger strong sweep events near the crest due to the competition between transverse-around flow and streamwise momentum transport. On the windward side in R5, the effect of transverse-around flow remains significant. Although the flow climbing over the crest decreases significantly, there is an overall increase in total streamwise momentum as the streamwise velocity rises. Consequently, the dispersive streamwise velocity weakens, as depicted in Fig. 15(a). This results in a narrower active DSS on the windward side, while its strength remains unaffected. Additionally, as shown in Fig. 15(b), the time-averaged vertical velocity decreases while the dispersive vertical velocity increases due to limitations on the flow path caused by climbing over the crest. With the interaction between the enhanced dispersive vertical and streamwise velocities, a dispersive ejection event emerges in R4.

Moreover, Figs. 15(b) and 15(d) demonstrate that the 3D wavy wall induces the occurrence of the  $Q_{d2}$  event in R2. In a 2D case, the flow separation is lifted on the leeward side, resulting in a positive value for the time-averaged vertical velocity. However, in the case of a 3D wavy wall,

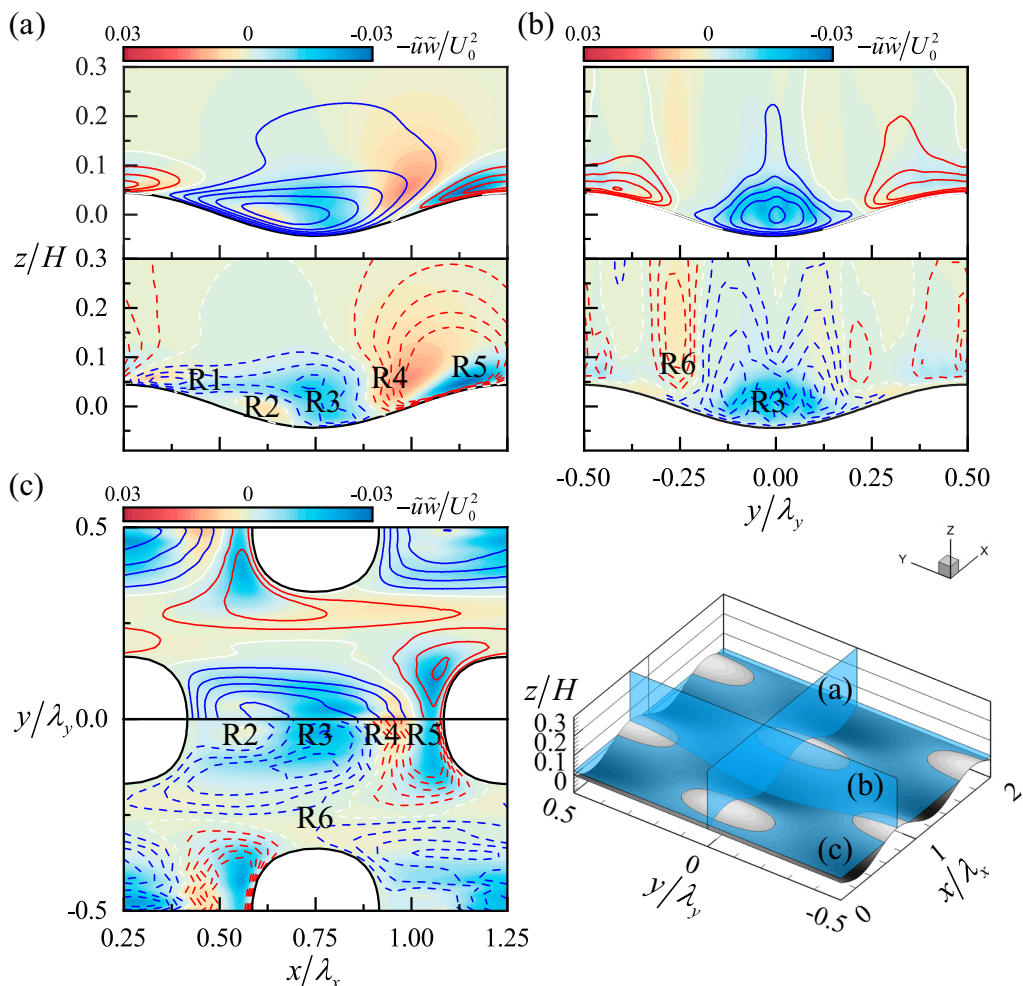


FIG. 14. The contours of dispersive shear stress (DSS) and isolines of dispersive velocity components for G2-6 on (a) YS1, (b) XS1, and (c) ZS1 sections. The solid and dashed lines are the dispersive streamwise and vertical velocities, with blue (red) denoting less (larger) than zero.

despite the weakened flow separation that would typically reduce the time-averaged vertical velocity of the reversed flow, the enhanced dispersive vertical velocity in R2 provides an alternative means of controlling the time-averaged vertical velocity. Omidyeganeh and Piomelli [11] noted the presence of secondary flows, or streamwise vortices, in turbulence over 3D dunes. In this context, we propose that the momentum transport induced by these secondary flows is responsible for activating flow dispersion in R2.

As mentioned in the previous section, the regions where the DSS is activated coincide with areas where velocity components exhibit notable characteristics. Medjnoun *et al.* [63] conducted experiments and discovered that DSS contributions are amplified by large-scale secondary flows, specifically streamwise vorticity, which are more pronounced near the core of these secondary flows. Chan *et al.* [64] also found that the secondary flow leads to a significant increase in dispersive stresses. This highlights the connection between local-averaged DSS and vorticity. In this paper, we have integrated the vorticity within the designated volume, resulting in the expression of

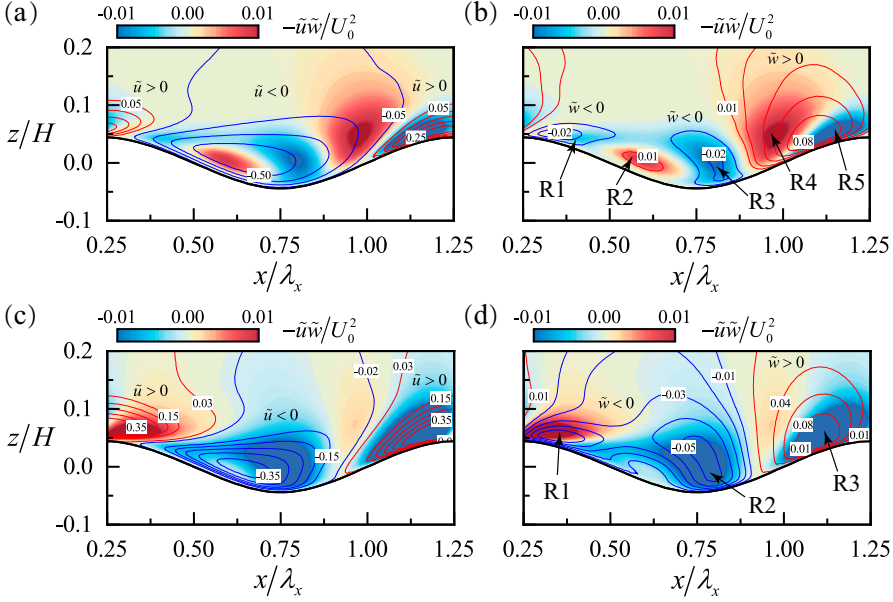


FIG. 15. Comparison of the dispersive shear stress (DSS) for (a) and (b) case G1-2 and (c) and (d) two-dimensional wavy wall case from our previous work [38]. The blue solid lines denote  $\tilde{u} < 0$  or  $\tilde{w} < 0$ , whereas the red solid lines represent  $\tilde{u} > 0$  or  $\tilde{w} > 0$ .

local-averaged streamwise, spanwise, and vertical vorticity as follows:

$$\begin{aligned}\Gamma_{\text{Iax}} &= \frac{1}{V} \int_0^{\lambda_x} \int_{-0.5\lambda_y}^{0.5\lambda_y} \int_{\eta}^{0.3H} |\tilde{\omega}_x| dx dy dz \\ \Gamma_{\text{Iay}} &= \frac{1}{V} \int_0^{\lambda_x} \int_{-0.5\lambda_y}^{0.5\lambda_y} \int_{\eta}^{0.3H} |\tilde{\omega}_y| dx dy dz \\ \Gamma_{\text{Iaz}} &= \frac{1}{V} \int_0^{\lambda_x} \int_{-0.5\lambda_y}^{0.5\lambda_y} \int_{\eta}^{0.3H} |\tilde{\omega}_z| dx dy dz,\end{aligned}\quad (14)$$

where  $V$  is the integral volume. Similarly, the local-averaged DSS is calculated by integrating the double-averaged DSS profiles, which can be determined by  $\tau_{\text{Iad}} = \frac{1}{0.3H} \int_0^{0.3H} \langle \bar{\tau}_d \rangle d(z)$ . Figure 16 illustrates the variation of local-averaged DSS as a function of the local-averaged vorticity components. Increasing the amplitude amplifies the streamwise and vertical vorticity, as depicted in Figs. 16(a) and 16(c). This amplification also leads to the growth of the DSS, indicating that the local-averaged DSS increases linearly with the enhancement of streamwise and vertical vorticity. This finding aligns with the observations of Medjnoun *et al.* [63], who reported a nearly linear relationship between DSS and circulation (defined as the integration of streamwise vorticity in their study). Notably, Fig. 16(b) shows that the spanwise vorticity decreases as the DSS increases, indicating that higher amplitudes limit the development of spanwise vorticity. This highlights the limited contribution of spanwise vorticity variation to the overall variation of DSS. However, for group 2 in Figs. 16(d)–16(f), a reversed trend emerges. Increasing the spanwise wavelength reduces both the local-averaged streamwise and vertical vorticity, yet the DSS is approximately strengthened. This suggests that the mechanism of streamwise-vortices-dominated DSS is no longer valid in this case. Figure 16(e) further demonstrates that the DSS increases linearly with the local-averaged spanwise vorticity, indicating the dominance of spanwise vortices in the variation of DSS. Therefore, the

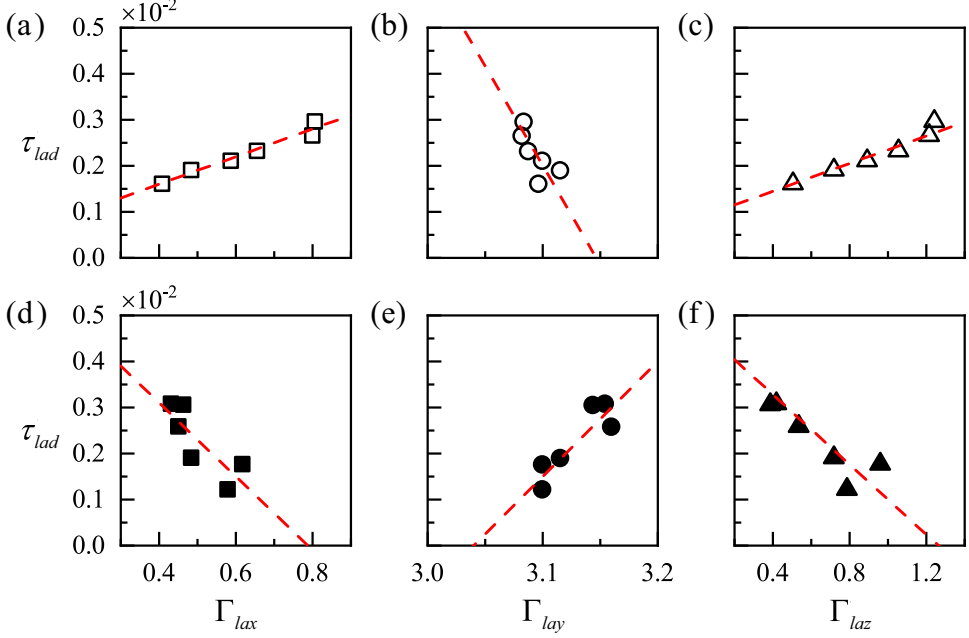


FIG. 16. Local-averaged dispersive shear stress (DSS) as a function of the local-averaged (a) and (d) streamwise, (b) and (e) spanwise, and (c) and (f) vertical vorticity for (a)–(c) group 1 and (d)–(f) group 2.

activation of DSS is closely related to vorticity variation. The amplitude variation primarily controls the DSS induced by streamwise vortices, while an increased spanwise wavelength affects DSS by adjusting the strength of spanwise vorticity.

#### D. Partition of the kinetic energy production

This section underlines the partition of kinetic energy production. According to the present temporal-spatial averaging decomposition, the conservation equation of the time-averaged kinetic energy can be deduced by multiplying the velocity components into the corresponding momentum equation. First, the time-averaged momentum conservation equation is

$$\frac{\partial \bar{u}_i}{\partial t} + \frac{\partial}{\partial x_j} (\bar{u}_i \bar{u}_j + \overline{u'_i u'_j}) = -\frac{1}{\rho} \frac{\partial \bar{p}}{\partial x_i} + \nu \frac{\partial^2 \bar{u}_i}{\partial x_j \partial x_j}. \quad (15)$$

Multiplying the time-averaged velocity gives

$$\bar{u}_i \frac{\partial \bar{u}_i}{\partial t} + \bar{u}_i \frac{\partial}{\partial x_j} (\bar{u}_i \bar{u}_j + \overline{u'_i u'_j}) = -\frac{1}{\rho} \frac{\partial \bar{p}}{\partial x_i} \bar{u}_i + \nu \frac{\partial^2 \bar{u}_i}{\partial x_j \partial x_j} \bar{u}_i. \quad (16)$$

Equation (16) can be rewritten as

$$\frac{D\bar{E}}{Dt} = \frac{\partial}{\partial x_j} \left( -\frac{\bar{p}\bar{u}_j}{\rho} - \bar{E}\bar{u}_j - \bar{u}_i \overline{u'_i u'_j} + 2\nu \bar{u}_i \bar{S}_{ij} \right) + \underbrace{\bar{u}_i \bar{u}_j \frac{\partial \bar{u}_i}{\partial x_j} + \overline{u'_i u'_j} \frac{\partial \bar{u}_i}{\partial x_j}}_{-P_t} - 2\nu \bar{S}_{ij} \bar{S}_{ij}, \quad (17)$$

where  $\bar{E} = \frac{1}{2} \bar{u}_i \bar{u}_i$  is the time-averaged kinetic energy, and  $\frac{D}{Dt} = \frac{\partial}{\partial t} + (\bar{\mathbf{u}} \cdot \nabla)$  is the material derivative,  $S_{ij}$  is the strain rate tensor, the term  $P_t = -\overline{u'_i u'_j} \frac{\partial \bar{u}_i}{\partial x_j}$  denotes the TKE production, and  $\bar{u}_i \bar{u}_j \frac{\partial \bar{u}_i}{\partial x_j}$  includes a term related to the dispersive kinetic energy (DKE) production, namely,  $P_d = -\bar{u}_i \bar{u}_j \frac{\partial \bar{u}_i}{\partial x_j}$ .

The TKE production represents the energy injection from the time-averaged flow into the turbulent motion, while the DKE production signifies the energy transfer from the time-averaged flow to flow dispersion. Equation (17) indicates that both turbulent and dispersive stresses contribute to the time-averaged kinetic energy production, implying that both the turbulent and dispersive stresses perform work on the time-averaged strain rate. The spatial averaging of Eq. (17) gives

$$\begin{aligned} \frac{D\langle\bar{E}\rangle}{Dt} &= \frac{\partial}{\partial x_j} \left( -\frac{\langle\bar{p}\bar{u}_j\rangle}{\rho} - \langle\bar{E}\bar{u}_j\rangle - \langle\bar{u}_i\overline{u'_i u'_j}\rangle + 2\nu\langle\bar{u}_i\bar{S}_{ij}\rangle \right) \\ &\quad + \left\langle \bar{u}_i\bar{u}_j \frac{\partial\bar{u}_i}{\partial x_j} \right\rangle + \underbrace{\left\langle \overline{u'_i u'_j} \frac{\partial\bar{u}_i}{\partial x_j} \right\rangle}_{-(P_t)} - 2\nu\langle\bar{S}_{ij}\bar{S}_{ij}\rangle. \end{aligned} \quad (18)$$

Then we conducted spatial averaging of Eq. (15) to obtain the mean momentum conservation equation:

$$\frac{\partial\langle\bar{u}_i\rangle}{\partial t} + \frac{\partial}{\partial x_j} (\langle\bar{u}_i\rangle\langle\bar{u}_j\rangle + \langle\tilde{u}_i\tilde{u}_j\rangle + \langle\overline{u'_i u'_j}\rangle) = -\frac{1}{\rho} \frac{\partial\langle\bar{p}\rangle}{\partial x_i} + \nu \frac{\partial^2\langle\bar{u}_i\rangle}{\partial x_j\partial x_j}. \quad (19)$$

Multiplying the mean velocity gives

$$\langle\bar{u}_i\rangle \frac{\partial\langle\bar{u}_i\rangle}{\partial t} + \langle\bar{u}_i\rangle \frac{\partial}{\partial x_j} (\langle\bar{u}_i\rangle\langle\bar{u}_j\rangle + \langle\tilde{u}_i\tilde{u}_j\rangle + \langle\overline{u'_i u'_j}\rangle) = -\frac{1}{\rho} \frac{\partial\langle\bar{p}\rangle}{\partial x_i} \langle\bar{u}_i\rangle + \nu \frac{\partial^2\langle\bar{u}_i\rangle}{\partial x_j\partial x_j} \langle\bar{u}_i\rangle. \quad (20)$$

Equation (20) can be rewritten as

$$\begin{aligned} \frac{DK}{Dt} &= \frac{\partial}{\partial x_j} \left( -\frac{\langle\bar{p}\rangle\langle\bar{u}_j\rangle}{\rho} - K\langle\bar{u}_j\rangle - \langle\bar{u}_i\rangle\langle\tilde{u}_i\tilde{u}_j\rangle - \langle\bar{u}_i\rangle\langle\overline{u'_i u'_j}\rangle + 2\nu\langle\bar{u}_i\rangle\langle\bar{S}_{ij}\rangle \right) \\ &\quad + \langle\bar{u}_i\rangle\langle\bar{u}_j\rangle \frac{\partial\langle\bar{u}_i\rangle}{\partial x_j} + \underbrace{\left\langle \tilde{u}_i\tilde{u}_j \frac{\partial\langle\bar{u}_i\rangle}{\partial x_j} \right\rangle}_{-(P_{md})} + \underbrace{\left\langle \overline{u'_i u'_j} \frac{\partial\langle\bar{u}_i\rangle}{\partial x_j} \right\rangle}_{-(P_{m})} - 2\nu\langle\bar{S}_{ij}\rangle\langle\bar{S}_{ij}\rangle, \end{aligned} \quad (21)$$

where  $K = \frac{1}{2}\langle\bar{u}_i\rangle\langle\bar{u}_i\rangle$  is the mean kinetic energy (MKE), the term  $\langle P_{m} \rangle = \langle -\overline{u'_i u'_j} \frac{\partial\langle\bar{u}_i\rangle}{\partial x_j} \rangle$  ( $\langle P_{md} \rangle = \langle -\tilde{u}_i\tilde{u}_j \frac{\partial\langle\bar{u}_i\rangle}{\partial x_j} \rangle$ ) represents the energy transfer between mean motion and turbulence (dispersion). Next, the dispersive momentum conservation equation can be derived through the difference between Eqs. (15) and (19), expressed as

$$\frac{\partial\tilde{u}_i}{\partial t} + \frac{\partial}{\partial x_j} (\bar{u}_i\bar{u}_j + \overline{u'_i u'_j} - \langle\bar{u}_i\rangle\langle\bar{u}_j\rangle - \langle\tilde{u}_i\tilde{u}_j\rangle - \langle\overline{u'_i u'_j}\rangle) = -\frac{1}{\rho} \frac{\partial\bar{p}}{\partial x_i} + \nu \frac{\partial^2\tilde{u}_i}{\partial x_j\partial x_j}. \quad (22)$$

Multiplying the dispersive velocity gives

$$\tilde{u}_i \frac{\partial\tilde{u}_i}{\partial t} + \tilde{u}_i \frac{\partial}{\partial x_j} (\bar{u}_i\bar{u}_j + \overline{u'_i u'_j} - \langle\bar{u}_i\rangle\langle\bar{u}_j\rangle - \langle\tilde{u}_i\tilde{u}_j\rangle - \langle\overline{u'_i u'_j}\rangle) = -\frac{1}{\rho} \frac{\partial\bar{p}}{\partial x_i} \tilde{u}_i + \nu \frac{\partial^2\tilde{u}_i}{\partial x_j\partial x_j} \tilde{u}_i. \quad (23)$$

The fluctuating momentum conservation equation is then considered:

$$\frac{\partial u'_i}{\partial t} + \frac{\partial}{\partial x_j} (u'_i\langle\bar{u}_j\rangle + u'_i\tilde{u}_j + \langle\bar{u}_i\rangle u'_j + \tilde{u}_i u'_j + u'_i u'_j - \overline{u'_i u'_j}) = -\frac{1}{\rho} \frac{\partial p'}{\partial x_i} + \nu \frac{\partial^2 u'_i}{\partial x_j\partial x_j}. \quad (24)$$

Multiplying the fluctuating velocity gives

$$u'_i \frac{\partial u'_i}{\partial t} + u'_i \frac{\partial}{\partial x_j} (u'_i\langle\bar{u}_j\rangle + u'_i\tilde{u}_j + \langle\bar{u}_i\rangle u'_j + \tilde{u}_i u'_j + u'_i u'_j - \overline{u'_i u'_j}) = -\frac{1}{\rho} \frac{\partial p'}{\partial x_i} u'_i + \nu \frac{\partial^2 u'_i}{\partial x_j\partial x_j} u'_i. \quad (25)$$

The spatial averaging of Eq. (23) and the time and spatial averaging of Eq. (25) yield the following energy conservation equations:

$$\begin{aligned} \frac{D\langle\bar{E}\rangle}{Dt} = & \frac{\partial}{\partial x_j} \left( -\frac{\langle\bar{p}\bar{u}_j\rangle}{\rho} - \langle\bar{u}_i\bar{u}_i\bar{u}_j\rangle - \langle\bar{u}_i\overline{u'_i u'_j}\rangle + 2\nu\langle\bar{u}_i\bar{S}_{ij}\rangle \right) \\ & + \underbrace{\left\langle \bar{u}_i\bar{u}_j \frac{\partial\bar{u}_i}{\partial x_j} \right\rangle}_{-(P_{dd})} + \underbrace{\left\langle \overline{u'_i u'_j} \frac{\partial\bar{u}_i}{\partial x_j} \right\rangle}_{-(P_{dt})} - \underbrace{\left\langle \bar{u}_i\bar{u}_j \frac{\partial\langle\bar{u}_i\rangle}{\partial x_j} \right\rangle}_{(P_{md})} - 2\nu\langle\bar{S}_{ij}\bar{S}_{ij}\rangle, \end{aligned} \quad (26)$$

$$\begin{aligned} \frac{D\langle\bar{E}'\rangle}{Dt} = & \frac{\partial}{\partial x_j} \left( -\frac{\langle\bar{p}'u'_j\rangle}{\rho} - \langle\overline{u'_i u'_j u'_j}\rangle - \langle\bar{E}'\bar{u}_j\rangle + 2\nu\langle\overline{u'_i S'_{ij}}\rangle \right) \\ & + \underbrace{\left\langle \overline{u'_i u'_j} \frac{\partial\bar{u}_i}{\partial x_j} \right\rangle}_{(P_{mt})} - \underbrace{\left\langle \overline{u'_i u'_j} \frac{\partial\langle\bar{u}_i\rangle}{\partial x_j} \right\rangle}_{(P_{dt})} - \underbrace{\left\langle \overline{u'_i u'_j} \frac{\partial\bar{u}_i}{\partial x_j} \right\rangle}_{(P_{dt})} - 2\nu\langle\overline{S'_{ij}S'_{ij}}\rangle, \end{aligned} \quad (27)$$

where  $\bar{E} = \frac{1}{2}\bar{u}_i\bar{u}_i$  is the DKE, and  $E' = \frac{1}{2}u'_i u'_i$  is the instantaneous TKE. Based on Eqs. (18), (21), (26), and (27), the terms associated with the TKE production ( $P_{mt}$ ) exhibit opposite signs in the conservation equations of MKE and TKE. This indicates the energy transfer occurring between the mean motion and turbulent motion. Similarly, the terms related to the DKE production ( $P_{md}$ ) also display opposite signs in the conservation equations of MKE and DKE, indicating the energy transfer between mean motion and flow dispersion. Notably, the term denoted as  $P_{dt}$  represents the work done by turbulent stresses on the dispersive velocity gradient, signifying the energy transfer between flow dispersion and the turbulent motion. The production terms are systematically distributed among the terms in the conservation equations of mean and dispersive kinetic energies. In other words, the TKE and DKE productions can be divided into

$$\begin{aligned} P_t &= -\overline{u'_i u'_j} \frac{\partial\bar{u}_i}{\partial x_j} = P_{mt} + P_{dt} = -\overline{u'_i u'_j} \frac{\partial\langle\bar{u}_i\rangle}{\partial x_j} - \overline{u'_i u'_j} \frac{\partial\bar{u}_i}{\partial x_j} \\ P_d &= -\bar{u}_i\bar{u}_j \frac{\partial\bar{u}_i}{\partial x_j} = P_{md} + P_{dd} = -\bar{u}_i\bar{u}_j \frac{\partial\langle\bar{u}_i\rangle}{\partial x_j} - \bar{u}_i\bar{u}_j \frac{\partial\bar{u}_i}{\partial x_j}. \end{aligned} \quad (28)$$

Here,  $P_t$  denotes the TKE production. The further spatial decomposition results in the mean TKE production  $P_{mt}$  and TKE-DKE exchange term  $P_{dt}$ , while  $P_d$  denotes the DKE production, and the further decomposition leads to the mean DKE production  $P_{md}$  and a term  $P_{dd}$  that is akin to energy transportation.

Figure 17 shows the production of TKE  $P_t$ , mean TKE  $P_{mt}$ , and TKE-DKE exchange  $P_{dt}$  on characteristic longitudinal and vertical sections ( $y/\lambda_y = 0$ ,  $z/a = 0.5$ ) for cases G1-2, G1-6, and G2-6. Here, the complete strain rate tensor is considered. The positive (negative) production terms indicate that the time-averaged flow is responsible for generating (suppressing) turbulence. From an energy transfer perspective, positive production terms signify that the time-averaged flow transfers energy into turbulence, while negative values indicate the other way around. Observing Figs. 17(a)–17(c) on the longitudinal sections, the TKE production becomes stronger with increasing amplitude and spanwise wavelength. Furthermore, Figs. 17(a)–17(c) illustrate that the TKE production is symmetrically distributed on the vertical sections, primarily generating turbulence behind the crest. Conversely, a negative TKE production is observed ahead of the crest, indicating the suppression of turbulence due to the growth of the internal boundary layer.

On the longitudinal section, the TKE components exhibit distinct behavior, as depicted in Figs. 17(d)–17(i). The leeward side is primarily governed by the negative (positive) production of mean TKE, whereas the windward side is dominated by the positive (negative) exchange between TKE and DKE. Notably, the TKE follows a similar pattern as the TKE-DKE exchange, indicating the significant role of wall heterogeneity in adjusting turbulence production. Moving to

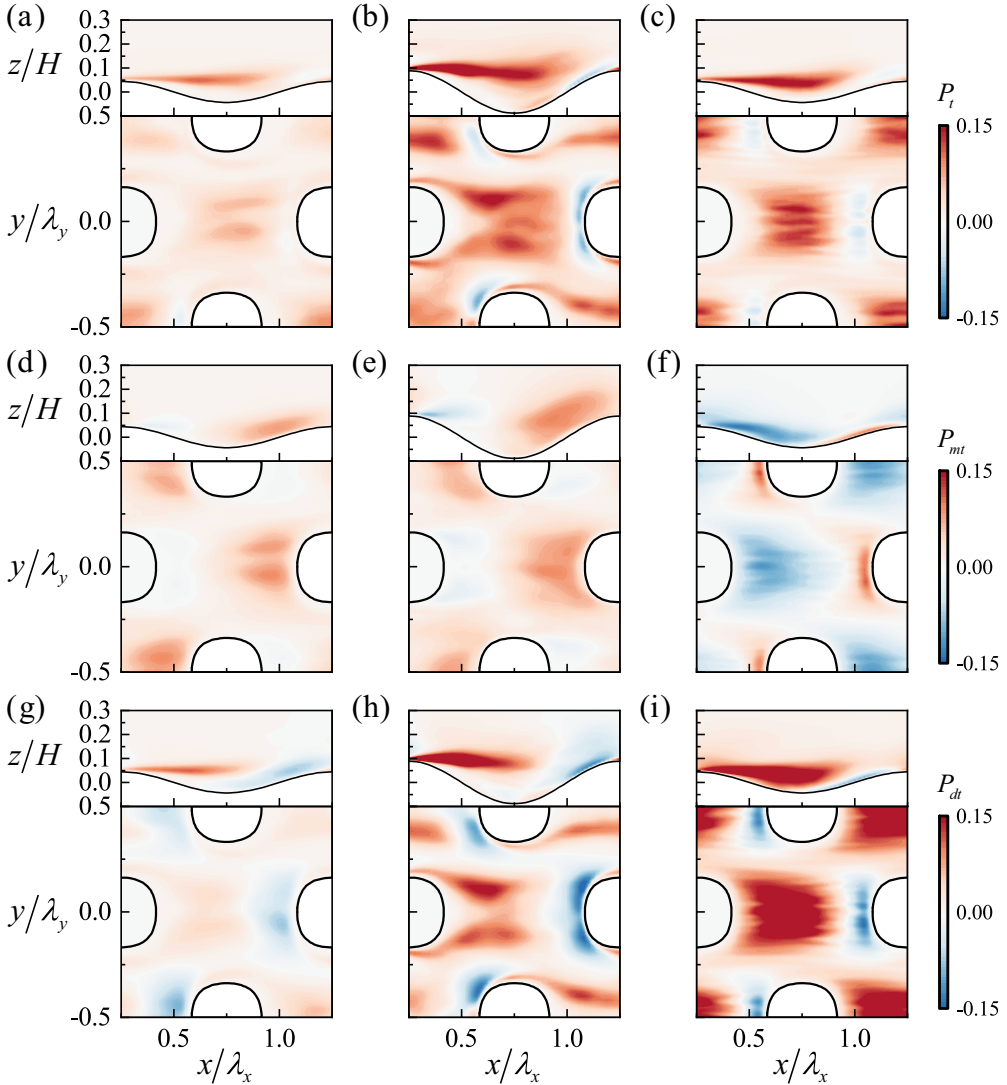


FIG. 17. (a)–(c) Turbulent kinetic energy (TKE) production, (d)–(f) mean TKE production, and (g)–(i) TKE-dispersive kinetic energy (DKE) exchange on longitudinal and vertical sections for cases (a), (d), and (g) G1-2, (b), (e), and (h) G1-6, and (c), (f), and (i) G2-6.

the vertical section, the mean TKE production is negative (positive) behind (ahead of) the crest, while the TKE-DKE exchange is positive (negative) in the same regions. Furthermore, the mean TKE makes a considerable contribution to TKE production in cases with small amplitudes, as seen in Figs. 17(a) and 17(d). However, for cases with high amplitudes or spanwise wavelengths, illustrated in Figs. 17(b), 17(c), 17(h), and 17(i), the TKE-DKE exchange predominantly controls TKE production. Overall, the mean TKE has a negative influence on TKE in most regions, while the TKE-DKE exchange positively governs TKE and plays a crucial role in enhancing TKE.

Figure 18 shows the production of DKE  $P_d$ , mean DKE  $P_{md}$ , and DKE transportation  $P_{dd}$  on characteristic longitudinal and vertical sections ( $y/\lambda_y = 0$ ,  $z/a = 0.5$ ) for cases G1-2, G1-6, and G2-6. The positive production terms indicate the transfer of energy from the time-averaged  $P$  flow to

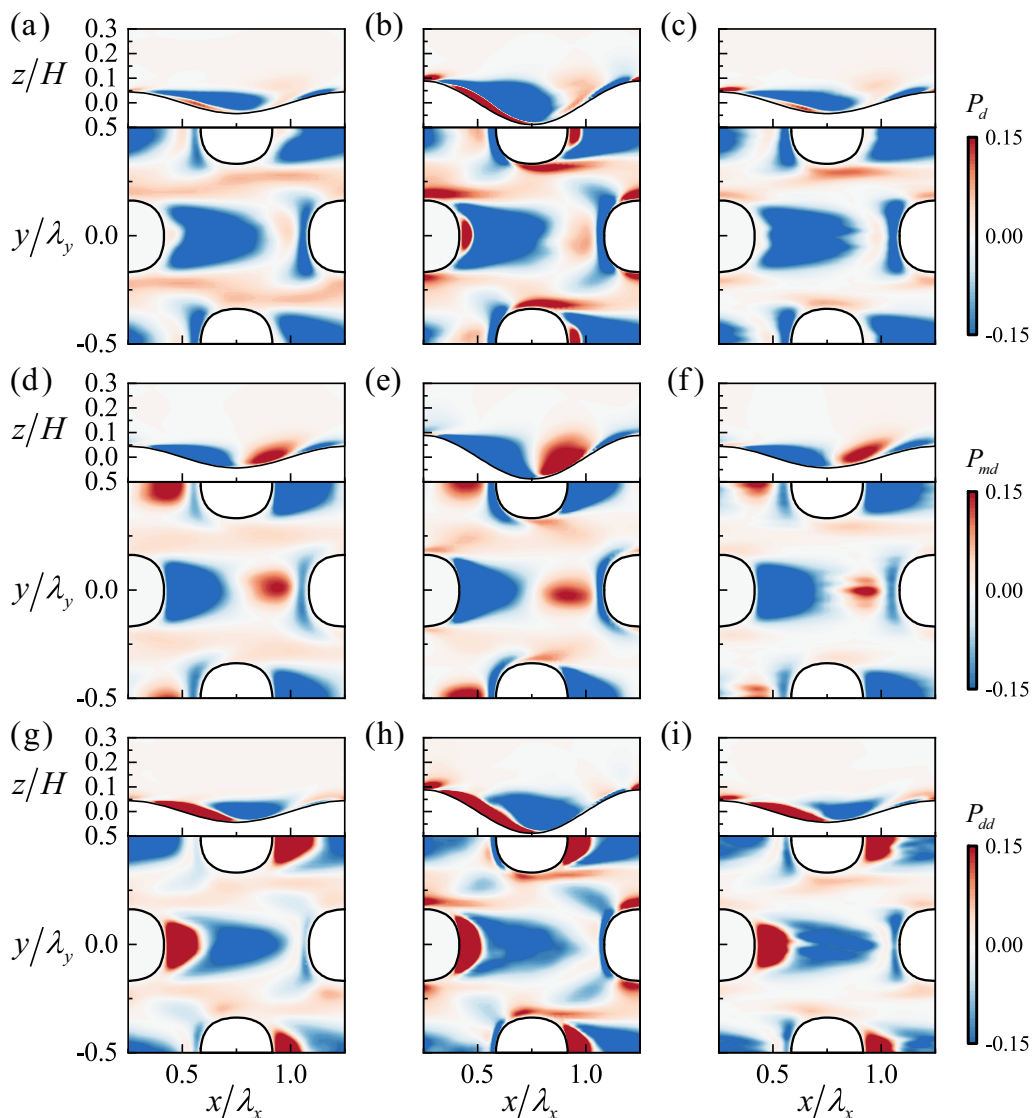


FIG. 18. (a)–(c) Dispersive kinetic energy (DKE) production, (d)–(f) mean DKE production, and (g)–(i) DKE transportation on longitudinal and vertical sections for cases (a), (d), and (g) G1-2, (b), (e), and (h) G1-6, and (c), (f), and (i) G2-6.

flow dispersion, while negative values represent the other way around. Examining the longitudinal section, as depicted in Figs. 18(a)–18(c), negative (positive) production terms are observed on the leeward (windward) side, indicating the generation (or suppression) of DKE by the time-averaged flow. The topography influences the DKE production, resulting in a complex pattern on the characteristic vertical section, as shown in Figs. 18(a)–18(c). In the case of G1-2 [Fig. 18(a)], positive DKE production is observed on both sides of the walls, extending downstream. This signifies the dispersion effect of the topographic protrusion on the time-averaged flow. However, behind the crest, a strong negative production term represents the convergence of dispersed flow into the averaged flow with the consumption of DKE energy. These characteristics are minimally affected by the shape



parameters considered, as demonstrated in the sections shown in Figs. 18(b) and 18(c). In cases with large amplitudes, such as case G1-6, a region very close to the crest exhibits positive DKE production, associated with enhanced streamwise flow separation. The reversed flow attached to the wall may disperse in the spanwise direction, thereby confirming the likely formation of streamwise vortices mentioned in Sec. IV C.

Figures 18(d)–18(i) show the mean DKE production and DKE transportation. The mean DKE production exhibits similar patterns to the DKE production in most regions. However, differences are observed in the small region behind the crest and ahead of the downstream crest (or the windward side). Notably, there is no positive mean DKE production behind the crest, in contrast with the positive DKE production shown in Figs. 18(a)–18(c). On the windward side, there is a noticeable enhancement in positive mean DKE production compared with weak positive DKE production. This indicates the presence of spatially heterogeneous velocity gradients. The distinction between mean DKE and DKE productions is balanced by the transportation of DKE. Figures 18(g)–18(i) suggest that flow dispersion amplifies the transportation of DKE. According to Eqs. (18) and (26), positive DKE transportation signifies the energy transfer from the time-averaged flow through dispersive motion into the mean flow, which is evident on the leeward side. Conversely, reversed transportation occurs on the windward side near the trough.

## V. CONCLUDING REMARKS

This paper contributes to the understanding of the impact of wall shape on turbulent statistics, specifically focusing on 3D wavy walls and their effects on momentum and kinetic energy transfer. Through extensive LESs, we have analyzed the influence of wall characteristics, such as amplitude and wavelength, on various turbulent parameters. The temporal-spatial averaging at relative height has been employed to unravel the macroscopic implications of the wall boundary on turbulent features, including velocity and vertical momentum flux profiles. Moreover, by deducing the kinetic energy balance equation, we have elucidated the underlying mechanisms of time-averaged, turbulent, and DKE productions.

The findings of this paper demonstrate that 3D wavy walls alter the transverse-around flow, leading to amplified effects on spanwise momentum flux and distinct patterns of spanwise momentum statistics. The presence of curved high-velocity streaks behind each crest supports these effects. Furthermore, the influence of wall shape parameters on momentum statistics components varies, with higher amplitudes enhancing all components, while increasing spanwise wavelengths weakens the spanwise momentum flux but strengthens the streamwise momentum flux, attributed to the reduction of transverse-around flow. The evaluation of the roughness function indicates that the cases with the highest amplitudes approximate the impact of full roughness on velocity profiles, while most cases fall within the transitionally rough regime. Additionally, the roughness function exhibits an increasing trend with rising amplitudes, while spanwise wavelength variations do not determine it. Notably, the roughness function adheres to the universal logarithmic law when evaluating the limiting spanwise-wavelength case (or the 2D wavy wall case with an equivalent amplitude).

The interplay between RSS and DSS plays a crucial role in determining the TSS (vertical momentum flux) in the near-wall region, highlighting the significance of DSS in controlling momentum transfer near the wall. The peak values of DSS profiles are dependent on the shape parameters, with increased amplitudes and spanwise wavelengths resulting in heightened DSS peaks. Moreover, the activation of DSS is superficially linked to the phase modulation between streamwise and vertical velocities, as evidenced by spatial quadrant analysis. However, the quadrant analysis reveals that a strong dispersive ejection behind the crest primarily originates from the probable generation of streamwise vortices. Building upon these findings, a correlation between locally averaged DSS and vorticity elucidates a more specific mechanism for activating DSS strength. The results indicate that increased amplitudes activate DSS through the enhancement of streamwise and vertical vorticity, while varying spanwise wavelengths influence DSS by adjusting the strength of spanwise vorticity.

The conservation equation of time-averaged kinetic energy reveals two distinct contributions to kinetic energy production: TKE and DKE production. The analysis shows that TKE production involves the transfer of energy from the time-averaged flow into turbulence, primarily influenced by the dispersive shear effect (or the TKE-DKE exchange), especially for high amplitude and spanwise-wavelength cases, thereby promoting spatially heterogeneous turbulence. In contrast, DKE production, resulting from the combined impact of temporal-spatial averaging and dispersive shear, diverges from TKE production. Most regions behind the crest facilitate the transfer of energy from flow dispersion into the time-averaged flow, indicative of flow convergence. Notably, the energy transferred from turbulence and dispersion into the mean flow on the windward side denotes the growth of the internal boundary layer. Additionally, positive DKE production in a narrow region near the crest can be attributed to flow reversal caused by separation, leading to dispersed vertical and spanwise flow due to the generation of streamwise vortices, as verified by quadrant analysis.

While in this paper we provide valuable insights into the influence of wall shape on turbulent statistics, there are still unanswered questions. The strong correlation between DSS and vorticity emphasizes the significant impact of vortex formation and interaction on momentum flux. Therefore, further exploration and in-depth discussions are warranted to elucidate how 3D wavy walls generate vortex structures and further affect the momentum transport. Additionally, future researchers should delve into the interaction between turbulent flow and sediment or particles, as it plays a crucial role in understanding river dynamics and the evolution of geomorphology in natural fluvial environments.

#### ACKNOWLEDGMENTS

The authors are grateful for support from the National Natural Science Foundation of China (Grants No. 12032005, No. 12302515, and No. 12325207) and the National Key R&D Program of China under Grant No. 2021YFA0719200.

- 
- [1] D. Ferraro, S. Servidio, V. Carbone, S. Dey, and R. Gaudio, Turbulence laws in natural bed flows, *J. Fluid Mech.* **798**, 540 (2016).
  - [2] G. Alfonsi, D. Ferraro, A. Lauria, and R. Gaudio, Large-eddy simulation of turbulent natural-bed flow, *Phys. Fluids* **31**, 085105 (2019).
  - [3] G. Sauermaun, P. Rognon, A. Poliakov, and H. J. Herrmann, The shape of the barchan dunes of Southern Morocco, *Geomorphology* **36**, 47 (2000).
  - [4] E. A. Zedler and R. L. Street, Large-eddy simulation of sediment transport: Currents over ripples, *J. Hydraul. Eng.* **127**, 444 (2001).
  - [5] N. Endo, K. Taniguchi, and A. Katsuki, Observation of the whole process of interaction between barchans by flume experiments, *Geophys. Res. Lett.* **31**, L12503 (2004).
  - [6] R. Fernandez, J. L. Best, and F. López, Mean flow, turbulence structure, and bed form superimposition across the ripple-dune transition, *Water Resour. Res.* **42**, W05406 (2006).
  - [7] W. S. Yue, C. L. Lin, and V. C. Patel, Large-eddy simulation of turbulent flow over a fixed two-dimensional dune, *J. Hydraul. Eng.* **132**, 643 (2006).
  - [8] D. G. E. Grigoriadis, E. Balaras, and A. A. Dimas, Large-eddy simulations of unidirectional water flow over dunes, *J. Geophys. Res.* **114**, F02022 (2009).
  - [9] M. Omidyeganeh, U. Piomelli, K. T. Christensen, and J. L. Best, Large eddy simulation of interacting barchan dunes in a steady, unidirectional flow, *J. Geophys. Res.-Earth* **118**, 2089 (2013).
  - [10] N. R. Bristow, G. Blois, J. L. Best, and K. T. Christensen, Turbulent flow structure associated with collision between laterally offset, fixed-bed barchan dunes, *J. Geophys. Res.-Earth* **123**, 2157 (2018).
  - [11] M. Omidyeganeh and U. Piomelli, Large-eddy simulation of three-dimensional dunes in a steady, unidirectional flow. Part 1. Turbulence statistics, *J. Fluid Mech.* **721**, 454 (2013).

- [12] L. Chan, M. MacDonald, D. Chung, N. Hutchins, and A. Ooi, A systematic investigation of roughness height and wavelength in turbulent pipe flow in the transitionally rough regime, *J. Fluid Mech.* **771**, 743 (2015).
- [13] W. M. Gong, P. A. Taylor, and A. Dornbrack, Turbulent boundary-layer flow over fixed aerodynamically rough two-dimensional sinusoidal waves, *J. Fluid Mech.* **312**, 1 (1996).
- [14] S. Leonardi, P. Orlandi, and R. A. Antonia, Properties of  $d$ - and  $k$ -type roughness in a turbulent channel flow, *Phys. Fluids* **19**, 125101 (2007).
- [15] E. Napoli, V. Armenio, and M. De Marchis, The effect of the slope of irregularly distributed roughness elements on turbulent wall-bounded flows, *J. Fluid Mech.* **613**, 385 (2008).
- [16] K. A. Flack and M. P. Schultz, Roughness effects on wall-bounded turbulent flows, *Phys. Fluids* **26**, 101305 (2014).
- [17] D. T. Squire, C. Morrill-Winter, N. Hutchins, M. P. Schultz, J. C. Klewicki, and I. Marusic, Comparison of turbulent boundary layers over smooth and rough surfaces up to high Reynolds numbers, *J. Fluid Mech.* **795**, 210 (2016).
- [18] P. Berghout, X. J. Zhu, D. Chung, R. Verzicco, R. J. A. M. Stevens, and D. Lohse, Direct numerical simulations of Taylor-Couette turbulence: The effects of sand grain roughness, *J. Fluid Mech.* **873**, 260 (2019).
- [19] T. Stoesser, C. Braun, M. García-Villalba, and W. Rodi, Turbulence structures in flow over two-dimensional dunes, *J. Hydraul. Eng.* **134**, 42 (2008).
- [20] K. Chang and G. Constantinescu, Coherent structures in flow over two-dimensional dunes, *Water Resour. Res.* **49**, 2446 (2013).
- [21] S. Naqshband, J. S. Ribberink, D. Hurther, and S. J. M. H. Hulscher, Bed load and suspended load contributions to migrating sand dunes in equilibrium, *J. Geophys. Res.-Earth* **119**, 1043 (2014).
- [22] C. A. Unsworth, D. R. Parsons, R. J. Hardy, A. J. H. Reesink, J. L. Best, P. J. Ashworth, and G. M. Keevil, The impact of nonequilibrium flow on the structure of turbulence over river dunes, *Water Resour. Res.* **54**, 6566 (2018).
- [23] P. A. Hesp and K. Hastings, Width, height and slope relationship and aerodynamic maintenance of barchans, *Geomorphology* **22**, 193 (1998).
- [24] P. Hersen and S. Douady, Collision of barchan dunes as a mechanism of size regulation, *Geophys. Res. Lett.* **32**, L21403 (2005).
- [25] J. A. Palmer, R. Mejia-Alvarez, J. L. Best, and K. T. Christensen, Particle-image velocimetry measurements of flow over interacting barchan dunes, *Exp. Fluids* **52**, 809 (2011).
- [26] E. J. R. Parteli, O. Duran, M. C. Bourke, H. Tsoar, T. Poschel, and H. J. Herrmann, Origins of barchan dune asymmetry: Insights from numerical simulations, *Aeolian Res.* **12**, 121 (2013).
- [27] C. Wang and W. Anderson, Large-eddy simulation of turbulent flow over spanwise-offset barchan dunes: Interdune vortex stretching drives asymmetric erosion, *Phys. Rev. E* **98**, 033112 (2018).
- [28] W. R. Assis and E. M. Franklin, A comprehensive picture for binary interactions of subaqueous barchans, *Geophys. Res. Lett.* **47**, e2020GL089464 (2020).
- [29] A. M. Hamed, M. Sadowski, Z. Zhang, and L. P. Chamorro, Transition to turbulence over 2D and 3D periodic large-scale roughness, *J. Fluid Mech.* **804**, R6 (2016).
- [30] J. G. Venditti, Bedforms in sand-bedded rivers, *Treatise on Geomorphology* **9**, 137 (2013).
- [31] J. G. Venditti and B. O. Bauer, Turbulent flow over a dune: Green River, Colorado, *Earth Surf. Proc. Land.* **30**, 289 (2005).
- [32] T. B. Maddux, J. M. Nelson, and S. R. McLean, Turbulent flow over three-dimensional dunes: 1. Free surface and flow response, *J. Geophys. Res.-Earth* **108**, 6009 (2003).
- [33] T. B. Maddux, S. R. McLean, and J. M. Nelson, Turbulent flow over three-dimensional dunes: 2. Fluid and bed stresses, *J. Geophys. Res.-Earth* **108**, 6010 (2003).
- [34] A. M. Hamed, A. Kamdar, L. Castillo, and L. P. Chamorro, Turbulent boundary layer over 2D and 3D large-scale wavy walls, *Phys. Fluids* **27**, 106601 (2015).
- [35] D. Pokrajac, L. J. Campbell, V. Nikora, C. Manes, and I. Mcewan, Quadrant analysis of persistent spatial velocity perturbations over square-bar roughness, *Exp. Fluids* **42**, 413 (2007).

- [36] J. M. Wallace, Quadrant analysis in turbulence research: History and evolution, *Annu. Rev. Fluid Mech.* **48**, 131 (2016).
- [37] S. Dey, P. Paul, and E. Padhi, Conditional spatially averaged turbulence and dispersion characteristics in flow over two-dimensional dunes, *Phys. Fluids* **32**, 065106 (2020).
- [38] E. W. Zhang, X. L. Wang, and Q. Q. Liu, Numerical investigation on the temporal and spatial statistical characteristics of turbulent mass transfer above a two-dimensional wavy wall, *Int. J. Heat Mass Trans.* **184**, 122260 (2022).
- [39] Y. Brunet, J. J. Finnigan, and M. R. Raupach, A wind tunnel study of air flow in waving wheat: Single-point velocity statistics, *Bound-Lay. Meteorol.* **70**, 95 (1994).
- [40] S. E. Coleman and V. I. Nikora, A unifying framework for particle entrainment, *Water Resour. Res.* **44**, W04415 (2008).
- [41] E. Mignot, E. Barthelemy, and D. Hurther, Double-averaging analysis and local flow characterization of near-bed turbulence in gravel-bed channel flows, *J. Fluid Mech.* **618**, 279 (2009).
- [42] S. Dey and R. Das, Gravel-bed hydrodynamics: Double-averaging approach, *J. Hydraul. Eng.* **138**, 707 (2012).
- [43] J. Yuan and U. Piomelli, Roughness effects on the Reynolds stress budgets in near-wall turbulence, *J. Fluid Mech.* **760**, R1 (2014).
- [44] C. D. Ghodke and S. V. Apte, DNS study of particle-bed-turbulence interactions in an oscillatory wall-bounded flow, *J. Fluid Mech.* **792**, 232 (2016).
- [45] A. Zampiron, S. Cameron, and V. Nikora, Momentum and energy transfer in open-channel flow over streamwise ridges, *J. Fluid Mech.* **915**, A42 (2021).
- [46] A. J. Raudkivi, *Loose Boundary Hydraulics* (Balkema, Rotterdam, 1998).
- [47] W. W. Kim and S. Menon, A new dynamic one-equation subgrid-scale model for large eddy simulations, *33rd Aerospace Sciences Meeting and Exhibit* (AIAA, Reno, 1995).
- [48] S. Ghosal, T. S. Lund, P. Moin, and K. Akselvoll, A dynamic localization model for large-eddy simulation of turbulent flows, *J. Fluid Mech.* **286**, 229 (1995).
- [49] S. H. Huang and Q. S. Li, A new dynamic one-equation subgrid-scale model for large eddy simulations, *Int. J. Numer. Meth. Eng.* **81**, 835 (2009).
- [50] E. W. Zhang, X. L. Wang, and Q. Q. Liu, Effects of the spanwise heterogeneity of a three-dimensional wavy wall on momentum and scalar transport, *Phys. Fluids* **33**, 055116 (2021).
- [51] E. W. Zhang, W. X. Wu, Q. Q. Liu, and X. L. Wang, Effects of vortex formation and interaction on turbulent mass transfer over a two-dimensional wavy wall, *Phys. Rev. Fluids* **7**, 114607 (2022b).
- [52] M. MacDonald, D. Chung, N. Hutchins, L. Chan, A. Ooi, and R. García-Mayoral, The minimal-span channel for rough-wall turbulent flows, *J. Fluid Mech.* **816**, 5 (2017).
- [53] C. Maass and U. Schumann, Numerical simulation of turbulent flow over a wavy boundary, in *Direct and Large-Eddy Simulation I. Fluid Mechanics and Its Applications*, edited by P. R. Voke, L. Kleiser, and J. P. Chollet (Springer, Dordrecht, 1994), Vol. 26, p. 287.
- [54] A. Nakayama and K. Sakio, Simulation of flows over wavy rough boundaries, Annual Research Briefs, Center for Turbulence Research 313 (2002).
- [55] J. Finnigan, Turbulence in plant canopies, *Annu. Rev. Fluid Mech.* **32**, 519 (2000).
- [56] V. Nikora, I. McEwan, S. McLean, S. Coleman, D. Pokrajac, and R. Walters, Double-averaging concept for rough-bed open-channel and overland flows: Theoretical background, *J. Hydraul. Eng.* **133**, 8 (2007).
- [57] J. D. Hudson, L. Dykhno, and T. J. Hanratty, Turbulence production in flow over a wavy wall, *Exp. Fluids* **20**, 257 (1996).
- [58] P. Cherukat, Y. Na, T. J. Hanratty, and J. B. McLaughlin, Direct numerical simulation of a fully developed turbulent flow over a wavy wall, *Theor. Comput. Fluid Dyn.* **11**, 109 (1998).
- [59] D. Yang and L. Shen, Characteristics of coherent vortical structures in turbulent flows over progressive surface waves, *Phys. Fluids* **21**, 125106 (2009).
- [60] F. R. Hama, Boundary-layer characteristics for smooth and rough surfaces, *Trans. Soc. Naval. Arch. Mar. Engrs* **62**, 333 (1954).
- [61] K. A. Flack and M. P. Schultz, Review of hydraulic roughness scales in the fully rough regime, *J. Fluid. Eng.* **132**, 041203 (2010).

- [62] J. Nikuradse, Laws of flow in rough pipes, (NACA, Washington, 1933).
- [63] T. Medjnoun, C. Vanderwel, and B. Ganapathisubramani, Effects of heterogeneous surface geometry on secondary flows in turbulent boundary layers, [J. Fluid Mech. 886, A31 \(2020\)](#).
- [64] L. Chan, M. MacDonald, D. Chung, N. Hutchins, and A. Ooi, Secondary motion in turbulent pipe flow with three-dimensional roughness, [J. Fluid Mech. 854, 5 \(2018\)](#).